Title: Plant mixed lineage kinase domain-like proteins limit biotrophic pathogen growth

One Sentence Summary: Plants have a protein family that is structurally homologous to vertebrate mixed lineage kinase domain-like protein, which induces necroptotic cell death, but these plant proteins can confer immunity without host cell death.

Short title: Plant MLKLs confer disease resistance

Authors: Lisa Mahdi*[1,2], Menghang Huang*[3], Xiaoxiao Zhang*[3], Ryohei Thomas Nakano[1,4], Leïla Brulé Kopp[1,5], Isabel M.L. Saur[1], Florence Jacob[1,6,7], Viera Kovacova[8,9], Dmitry Lapin[1], Jane E. Parker[1,4], James M. Murphy[10,11], Kay Hofmann[12], Paul Schulze-Lefert[1,4], Jijie Chai[1,3,4] and Takaki Maekawa[1, †]

*These authors contributed equally
[1]Max Planck Institute for Plant Breeding Research, 50829 Cologne, Germany
[2]Current address, Botanical Institute, Cologne Biocenter, University of Cologne, Cologne, 50674, Germany.
[3]Beijing Advanced Innovation Center for Structural Biology, Tsinghua-Peking Joint Center for Life Sciences, Center for Plant Biology, School of Life Sciences, Tsinghua University, 100084 Beijing, China.
[4]Cluster of Excellence on Plant Sciences (CEPLAS), Max Planck Institute for Plant Breeding Research, 50829 Cologne, Germany
[5]Ecole normale supérieure Paris, F-75230 Paris cedex 05
[6]Institute of Plant Sciences Paris-Saclay, Centre National de la Recherche Scientifique, Institut National de la Recherche Agronomique, Université Paris-Sud, Université d'Evry, Université Paris-Diderot, Sorbonne Paris-Cité, Université Paris-Saclay, 91405 Orsay, France
[7]Current address, PalmElit SAS, F-34980 Montferrier-sur-Lez, France
[8]University of Cologne, Cologne Excellence Cluster on Cellular Stress Responses in Aging-Associated Diseases (CECAD), University of Cologne, 50931 Cologne, Germany.
[9]Current address: Institute for Biological Physics, University of Cologne, Cologne, 50937, Germany.
[10]Walter and Eliza Hall Institute of Medical Research, 1G Royal Parade, Parkville, VIC 3052, Australia;
[11]Department of Medical Biology, University of Melbourne, Parkville, VIC 3052, Australia.
[12]Institute for Genetics, University of Cologne, 50674 Cologne, Germany
[†]Corresponding author. Email: maekawa@mpipz.mpg.de (T.M.)

Abstract:

Mixed lineage kinase domain-like (MLKL) protein mediates necroptotic cell death in vertebrates. We report here the discovery of a conserved protein family across seed plants that is structurally homologous to vertebrate MLKL. The *Arabidopsis thaliana* genome encodes three MLKLs with overlapping functions in limiting growth of obligate biotrophic fungal and oomycete pathogens. Although displaying a cell death activity mediated by N-terminal helical bundles, termed HeLo domain, *At*MLKL-dependent immunity can be separated from host cell death. Cryo-electron microscopy structures of *At*MLKLs reveal a tetrameric configuration, in which the pseudokinase domain and brace region bury the HeLo-domains, indicative of an auto-repressed complex. We also show the association of two *At*MLKLs with microtubules. These findings, coupled with resistance-enhancing activity and altered microtubule association of a phosphomimetic mutation in the pseudokinase domain of *At*MLKL1, point to a cell death-independent immunity mechanism.

Main text:

Regulated cell death (RCD) is intimately connected with innate immunity in plants and animals (*1-3*). A shared feature of several proteins involved in RCD in plants, animals and fungi is a four-helical bundle structure called the HeLo-domain (*4*). HeLo domain-containing MLKL (mixed lineage kinase domain-like protein) mediates necroptosis in animals (*5, 6*), a form of RCD that is proposed to combat pathogens by releasing pro-inflammatory molecules (*7, 8*). Necroptosis is initiated by the plasma membrane (PM)-resident death receptors, with downstream activation of receptor-interacting serine/threonine-protein kinases (RIPKs) leading to the phosphorylation of the pseudokinase domain of the terminal pathway effector, MLKL (*7, 8*). This process assembles monomeric MLKL into pro-necroptotic oligomers (*9*) that translocate to the PM where oligomerized HeLo-domains interfere with membrane integrity (*10-14*). The extent to which RCD in plants and animals is directly responsible for disease resistance is under debate (*3, 15-17*).

To identify novel immune regulators in plants, we searched for HeLo domain-containing proteins in plant genomes by comparing Hidden Markov Models. This analysis identified a protein family that is highly conserved across plants (Fig. 1, Table S1, Supplemental file 1), with a modular structure resembling MLKL (Fig. 1A). The kinase-like domain lacks canonical residues known to underlie phosphoryl transfer (*18*) (Fig. 1B), suggestive of a catalytically inactive pseudokinase (*8*). Hereafter, we refer to these proteins as plant MLKLs. Plant MLKLs additionally possess an extended serine-rich region of varying length after the pseudokinase domain without similarity to any known

74 domain (Fig. 1A, Supplemental file 1). Plant MLKLs separate into two
75 subgroups based on sequence similarity (Fig. 1D). *Arabidopsis thaliana*
76 harbours three *MLKL* genes with *AtMLKL1* and *AtMLKL2* in subfamily I and
77 *AtMLKL3* belonging to subfamily II (Fig. 1D).

78

79 To explore similarities between plant and animal MLKLs, we expressed
80 *At*MLKL2 and *A*tMLKL3 for structural analysis using cryo-electron microscopy
81 (Fig. 2, Fig. S1 and S2). In gel filtration, both proteins eluted at an estimated
82 molecular weight corresponding to tetramers (Fig. 2A, Fig. S2A). This
83 contrasts with the vertebrate MLKL protein, which displayed heterogeneity in
84 a similar assay (*13*). Representative 2D projection views indicate that both
85 *At*MLKL oligomers form a triangle-like architecture with a 2-fold symmetry (Fig.
86 S1AB, Fig. S2BC). Further 3D classification and refinement generated density
87 maps of oligomeric *At*MLKL2 and *At*MLKL3 with a global resolution of 4.1Å
88 (Fig. S2E) and 3.4Å (Fig. S1D) respectively, based on the gold Fourier Shell
89 Correlation standard (Fig. S1C, Fig. S2D). The 3D reconstructions show that
90 both *At*MLKL2 and *At*MLKL3 oligomers are composed of four MLKL
91 molecules (Fig. 2C, Fig. S3A), confirming that these form tetramers.
92 Tetramerization of *At*MLKL2 or *At*MLKL3 results in formation of a pyramid-like
93 structure. Structure alignment of the two final models indicates that tetramers
94 of two subfamily members are nearly identical (Fig. S3AB). As the quality of
95 the density of *At*MLKL3 is superior for model building, we limited our structural
96 analysis to *At*MLKL3.

97 The N-terminal HeLo domain of *At*MLKL3 forms a four-helix bundle (Fig. S3C)
98 which superimposed well with the HeLo domains of mouse and human MLKL
99 (mMLKL and hMLKL, respectively; Fig. 2D). This observation supports the
100 idea that *At*MLKL3 is a bona fide homolog of vertebrate MLKLs. Nevertheless,
101 compared to mMLKL, the HeLo domain of *At*MLKL3 packs tightly against its
102 pseudokinase domain (Fig. S3D). The packing is further strengthened by the
103 brace region of *At*MLKL3, which contains a string of five helices that
104 simultaneously interact with the HeLo and pseudokinase domains (Fig. S3C).
105 The HeLo domains and the brace regions form the core of the *At*MLKL3
106 tetramer, whereas the pseudokinase domains are presented at the apices of
107 the pyramid-like structure (Fig. 2C). Hydrophobic packing of α1 helices (Fig.
108 S3E) from two *At*MLKL3 molecules contributes to formation of a homodimeric
109 *At*MLKL3. In the tetrameric *At*MLKL3, the two α1-mediated homodimers pack
110 perpendicularly to each other (Fig. 2G). Four brace regions, which are
111 positioned nearly in the same plane, are sandwiched between the two
112 homodimers and exclusively mediate homodimer-homodimer interaction (Fig.
113 2F). The N-terminal halves of the four brace regions form two homodimer
114 pairs, and the C-terminal halves another two pairs (Fig. S3E). The
115 intermolecular interactions lead to further sequestering of the *At*MLKL3 N-
116 terminal HeLo domain. Taken together, our observations indicate that
117 *At*MLKL3 is a structural homolog of vertebrate MLKLs and its N-terminal HeLo
118 domain is sequestered through both intra- and intermolecular interactions.

119

120 To determine the role of plant MLKLs in immunity, we challenged
121 combinatorial loss-of-function mutants of *At*MLKLs (Fig. S4) with different

122 microbial pathogens. *Atmlkl* single mutants exhibited increased susceptibility
123 to the obligate biotrophic fungus *Golovinomyces orontii* compared to wild-type
124 plants and, strikingly, the triple mutant was as susceptible as an *eds1* mutant
125 (Fig. 3A), which is hyper-susceptible to a number of pathogens including the
126 obligate biotrophic oomycete *Hyaloperonospora arabidopsidis* (*Hpa*). The
127 immune response restricting *Golovinomyces* growth in Col-0 wild-type plants
128 is not associated with host cell death (*19*). In *A. thaliana*, immunity to *Hpa*
129 isolate Emwa1 is mediated by RPP4, an NLR that requires EDS1 for function
130 (*20*). RPP4-mediated disease resistance was partially compromised in the
131 *Atmlkl* triple mutant, as measured by increased *Hpa* sporangiophore formation
132 on true leaves (Fig. 3B). We did not detect marked differences between the
133 susceptibility of wild-type and mutant plants to hemi-biotrophic *Pseudomonas*
134 *syringae* pv. *tomato* DC3000 bacteria or the fungal necrotroph *Botrytis cinerea*
135 (Fig. S5AB). Furthermore, disease resistance mediated by RPS2 and cell
136 death mediated by RPM1 NLRs were largely retained in the *Atmlkl123* mutant
137 (Fig. S5CD).

138

139 RNA-seq analysis using mock- and *G. orontii*-challenged leaves of wild-type,
140 *Atmlkl23, Atmlkl123* and *eds1* lines showed that the *AtMLKL1* transcript was
141 induced upon pathogen challenge (7.4 fold) and that induction was fully
142 dependent on *EDS1* (Fig. 3C, Fig. S6). Further analysis revealed that
143 *At*MLKLs regulate transcriptional reprogramming both under unchallenged
144 conditions and upon pathogen attack (Fig. 3C). These data imply a specific
145 and partly redundant role of *At*MLKLs in resistance to obligate biotrophic
146 pathogens.

147

148 To test whether *At*MLKLs possess cell death activity, possibly regulated by
149 phosphorylation, we introduced single phosphomimetic substitutions at serine
150 residues in the activation loops of *At*MLKLs (Fig. 1B) and expressed in *A.*
151 *thaliana* leaf protoplasts (see method). Upon overexpression, all wild-type
152 *At*MLKLs elicited cell death, which was as potent as an N-terminal barley NLR
153 cell death module (*21*)(Fig. S7). We found that a phosphomimetic substitution
154 at serine^{393} but not serine^{395} in *At*MLKL1 enhanced its cell-killing activity (Fig.
155 4A). However, an alanine substitution at serine^{393} did not compromise the cell
156 death activity, suggesting that other serine or threonine residues in the
157 activation loop (Fig. 1B) have a compensatory function. Using transgenic *A.*
158 *thaliana* lines, we observed that the enhanced susceptibility of *Atmlkl1* and
159 *Atmlkl2* mutants to *G. orontii* was restored by stable transformations of
160 genomic fragments encompassing wild-type *AtMLKL1* and *AtMLKL2*,
161 respectively (Fig. 4B,C and Fig. S8-9). In line with the protoplast assay (Fig.
162 4A), *At*MLKL1 (S393D) transgenic plants exhibited enhanced resistance to *G.*
163 *orontii* compared to Col-0 wild type, plants expressing the transgenes
164 *At*MLKL1 or *At*MLKL1 (S395D) (Fig. 4B,C). Unexpectedly, *At*MLKL1 (S393D)
165 transgenic plants did not exhibit cell death lesions or apparent plant growth
166 retardation indicative of autoimmunity (Fig. 4B, Fig. S8A). Collectively our
167 results suggest that plant MLKL function is in part regulated by activation loop
168 conformation, similar to vertebrate MLKLs (*22*), but *At*MLKL1 activity needed
169 to restrict *G. orontii* growth can be separated from host cell death.

170

171

172 We next examined whether the *At*MLKL N-terminal HeLo domain contributes
173 to its cell death activity, as in animals (*8, 12, 14, 23*). Taking advantage of a
174 chemically enforced oligomerization system (Fig. S10, see method), we found
175 that expression of the HeLo domains with the brace region of *At*MLKL1 and
176 *At*MLKL3 was sufficient for cytotoxic activity and this activity was further
177 enhanced upon oligomerization (Fig. S10D). This finding mirrors the activity
178 of the HeLo domains with the brace region of MLKL (*14*) and is consistent
179 with our structure-based hypothesis that the full-length MLKL tetramer with
180 buried HeLo domains represents an inactive form (Fig. 2).

181

182 As animal MLKL translocates to the PM upon activation (*10-14*) we examined
183 whether GFP-tagged *At*MLKL variants associate with the PM using time-
184 resolved confocal microscopy. We detected mobile punctate signals in the
185 cytoplasmic space for all *At*MLKL1 variants (Fig. 4DE). Reduced mobility for a
186 fraction of *At*MLKL1-GFP signals when proximal to the PM (Fig. 4E) is
187 consistent with PM association. Intriguingly, maximum projection of the time-
188 lapse images revealed that *At*MLKL1 (wild type)-GFP, the S395D mutant
189 moved along filamentous structures (Fig. 4E, Supplemental movies 1 and 3;
190 Fig. S11A). These filamentous structures specifically colocalized with the
191 microtubule marker (*24*) mCherry-MAP4 (Fig. S11B-C), and association was
192 detectable upon *G. orontii* invasion (Fig. S12). Intriguingly, no filamentous
193 structures were detected in the S393D phosphomimetic line despite the
194 presence of a microtubule array (Fig. S13). These data suggest that specific

195 phosphorylation modulates the intracellular localization and activities of
196 *At*MLKL1 via cytoskeletal association.

197

198 The plant MLKL family described here is a first example of a non-receptor
199 immunity component consisting of multiple domains that is structurally shared
200 between animal and plants. MLKLs in these two kingdoms are likely products
201 of convergent evolution because their exon-intron structures are unrelated (~4
202 and 11 exons in *At*MLKLs and hMLKL, respectively). Our work serves as a
203 template to test structural predictions implicating the presence of a HeLo-
204 domain fold in a number of plant modular proteins, including the ADR1 family
205 of NLRs (*4, 25-27*). Despite the cell death activity of a putative HeLo-domain
206 of ADR1 (*28*), this family confers disease resistance without apparent host cell
207 death (*29*). This resembles *At*MLKL-mediated defense in wild-type plants to
208 *G. orontii* without host cell death, although *At*MLKLs have the capacity to
209 elicit cell death. These results raise the question of whether host defence and
210 cell death functions can be further disentangled in animal necroptosis
211 signalling.

212

212 **Fig. 1: Plant genomes encode structural homologs of MLKL.**

213 **A**, A diagram of plant and animal MLKLs. A variably sized serine-rich region
214 that has no similarity to known structures is directly C-terminal to the
215 pseudokinase domain of plant MLKLs.

216 **B**, Alignments of the four helical bundles (HeLo domain) and the
217 pseudokinase domains of *A. thaliana* MLKLs (*At*MLKLs) and representative
218 vertebrates. Invariant residues and conservative substitutions in > 50% of the
219 sequences are shown in light blue and grey backgrounds, respectively. The
220 residues responsible for the activation of human or mouse MLKL upon
221 phosphorylation are indicated in the red box. The serine residues examined in
222 this study are shown in red.

223 **C,** Plant MLKL-encoding genes across representative plant species. A full list
224 of MLKL-encoding genes in the genomes of 48 seed plants is shown in Table
225 S1.

226 **D**, Phylogenetic relationship of plant MLKLs. Neighbor-net analysis
227 discriminates two subgroups of plant MLKLs colored in light blue and orange
228 with bootstrap support of 0.85 (1,000 bootstrap replicates).

229

230 **Fig. 2. Structure of the *At*MLKL3 tetramer.**

231 **A,** Top: Gel filtration profiles of *At*MLKL3. Position of standard molecular
232 weight is indicated by arrow. Bottom: Peak fractions on the top were verified
233 by reducing SDS-PAGE with Coomassie Blue staining.
234
235 **B**, Final EM density map of the *At*MLKL3 tetramer. Local resolution of the
236 density map is shown on the right with scale indicated by colors, in angstroms.
237
238 **C**, Top: Final 3D reconstruction of *At*MLKL3 tetramer shown in three
239 orientations. Each monomer of *At*MLKL3 is shown in different colors. Bottom:
240 Cartoon shows the overall structure of *At*MLKL3 tetramer in three orientations.
241 Subdomains of *At*MLKL3 are shown in different colors.
242
243 **D** Superposition of the HeLo domains of *At*MLKL3 (yellow, PDB ID code
244 6KA4), human MLKL (blue, PDB ID code 2MSV) and mouse MLKL (Pink,
245 PDB ID code 4BTF). RMSD between *At*MLKL3 and mMLKL:3.745, RMSD
246 between *At*MLKL3 and hMLKL:4.010.

247
248 **E**, Electrostatic surface of HeLo domains of *At*MLKL3, human MLKL and
249 mouse MLKL in two orientations.
250

251 **F**, Cartoon shows the brace region of the *At*MLKL3 tetramer. Each monomer
252 of *At*MLKL3 is shown in different colors.

253 **G**, Cartoon shows the HeLo domains of the *At*MLKL3 tetramer in two
254 orientations. Each monomer of *At*MLKL3 is shown in different colors.

255

256 **Fig. 3: Arabidopsis MLKLs confer resistance to powdery and downy**
257 **mildew pathogens.**

258 **A,** *Atmlkl* mutants are susceptible to the powdery mildew *Golovinomyces*
259 *orontii* (arrowheads). Quantification of *G. orontii* DNA at seven days after
260 inoculation is relative to the corresponding Col-0 samples. (n=3, Tukey HSD
261 *$p < 0.05$).

262 **B,** The *Atmlkl* triple mutant is susceptible to the downy mildew
263 *Hyaloperonospora arabidopsidis*. The number of *Hpa* spores per gram fresh
264 weight of plants is presented. Data were obtained in three independent
265 experiments, each including two biological replicates (n=6). Asterisks indicate
266 significant differences (Tukey HSD $p < 0.05$). The 1st or 2nd true leaves were
267 stained with trypan blue to visualise hyphae growth. Sporangiophores were
268 formed on the true leaves of the *Atmlkl* triple mutant (black arrowheads).

269 **C,** Principal component analysis (PCA) of RNA-seq data from mock- and
270 pathogen-challenged leaves collected at 48 hours post *G. orontii* inoculation.

271 *WT is a segregant line derived from the cross between *Atmlkl1* and *Atmlkl3*.
272 The *eds1* mutant was used as a susceptible control.

273

274 **Fig. 4: Cell death activity, disease resistance and subcellular localization**
275 **of phosphomimetic *At*MLKL1 variants.**

276 **A,** A phosphomimetic substitution in *At*MLKL1 elicited enhanced cell death in
277 *Arabidopsis* mesophyll protoplasts. Luciferase and *At*MLKL1 expression
278 constructs were co-transfected into protoplasts and luciferase activity was
279 measured as a proxy of cell viability at 16 hours post transfection. The
280 positions of serine-to-aspartate residues are indicated in Fig. 1B. The C-
281 terminally HA-tagged variants were expressed under the control of the
282 constitutive cauliflower mosaic virus 35S promoter. (n=3, Tukey HSD *$p <$
283 0.01).

284 **B,** Macroscopic phenotype of transgenic *Arabidopsis* expressing
285 phosphomimetic variants of *At*MLKL1 in response to *G. orontii* (arrowheads).
286 Plants were photographed seven days after pathogen challenge.

287 **C,** Quantification of *G. orontii* DNA in infected leaves of transgenic plants at
288 14 days after pathogen challenge (n=4, Tukey HSD *$p < 0.05$).

289 **D,** Schematic diagram of the confocal images shown in **B**. The white circle
290 indicates GFP signal proximal to the PM.

291 **E**, Confocal images of the abaxial epidermis of the *Arabidopsis* transgenic
292 lines expressing phosphomimetic and wild-type variants of *At*MLKL1. GFP
293 signals indicated by white circles were immobile in the examined time period.
294 The corresponding movies are available as supplemental movies 1-3. The
295 asterisk indicates plastidial autofluorescence. Scale bars = 5 µm.

296

Acknowledgments: We thank the Max Planck Genome Centre Cologne for RNA-Seq and Petra Köchner, Sabine Haigis and Makoto Yoshikawa-Maekawa for technical assistance and Neysan Donnelly for editing the manuscript. We also thank Hirofumi Nakagami, Ton Timmers, Hamid Kashkar and Manolis Pasparakis for helpful suggestions. We also thank Takashi Hashimoto and Stefanie Sprunck for the mcherry-MAP4 and tagRFP-T-Lifeact vectors, respectively.

Data and materials availability: All data underlying the study are deposited at Protein Data bank (PDB): https://www.rcsb.org/) or Gene Expression Omnibus (GEO) database (https://www.ncbi.nlm.nih.gov/geo/).

Author contributions: T.M. conceptualized the project; L.M., M.H., X.Z., R.T.N., L.B.K., I.M.L.S., F.J., V.K., D.L., K.H., T.M. performed the investigations. J.P. J.M.M., P.S-L. J.C. T.M. validated the data, J.P. J.M.M., P.S-L. J.C. T.M. supervised the work, J.C. and T.M. wrote the original draft of the manuscript, J.P. P.S-L., J.M.M. reviewed and edited the manuscript.

Competing interests: The authors declare no competing interests.

Data and materials availability: All data needed to replicate the work are deposited in the Protein Data Bank (PDB) or Gene Expression Omnibus (GEO) database. Plants and plasmids described in the manuscript are available upon request.

316 **References**

317 1. N. S. Coll, P. Epple, J. L. Dangl, Programmed cell death in the plant
318 immune system. *Cell Death Differ* **18**, 1247-1256 (2011).
319 2. W. G. van Doorn, Classes of programmed cell death in plants,
320 compared to those in animals. *J Exp Bot* **62**, 4749-4761 (2011).
321 3. F. K. Chan, N. F. Luz, K. Moriwaki, Programmed necrosis in the cross
322 talk of cell death and inflammation. *Annu Rev Immunol* **33**, 79-106
323 (2015).
324 4. A. Daskalov *et al.*, Identification of a novel cell death-inducing domain
325 reveals that fungal amyloid-controlled programmed cell death is related
326 to necroptosis. *Proc Natl Acad Sci U S A* **113**, 2720-2725 (2016).
327 5. L. Sun *et al.*, Mixed lineage kinase domain-like protein mediates
328 necrosis signaling downstream of RIP3 kinase. *Cell* **148**, 213-227
329 (2012).
330 6. J. Zhao *et al.*, Mixed lineage kinase domain-like is a key receptor
331 interacting protein 3 downstream component of TNF-induced necrosis.
332 *Proc Natl Acad Sci U S A* **109**, 5322-5327 (2012).
333 7. T. Vanden Berghe, A. Linkermann, S. Jouan-Lanhouet, H. Walczak, P.
334 Vandenabeele, Regulated necrosis: the expanding network of non-
335 apoptotic cell death pathways. *Nat Rev Mol Cell Biol* **15**, 135-147
336 (2014).
337 8. E. J. Petrie, P. E. Czabotar, J. M. Murphy, The Structural Basis of
338 Necroptotic Cell Death Signaling. *Trends Biochem Sci* **44**, 53-63 (2019).
339 9. E. J. Petrie, J. M. Hildebrand, J. M. Murphy, Insane in the membrane: a
340 structural perspective of MLKL function in necroptosis. *Immunol Cell*
341 *Biol* **95**, 152-159 (2017).
342 10. X. Chen *et al.*, Translocation of mixed lineage kinase domain-like
343 protein to plasma membrane leads to necrotic cell death. *Cell Res* **24**,
344 105-121 (2014).
345 11. Y. Dondelinger *et al.*, MLKL compromises plasma membrane integrity
346 by binding to phosphatidylinositol phosphates. *Cell Rep* **7**, 971-981
347 (2014).
348 12. J. M. Hildebrand *et al.*, Activation of the pseudokinase MLKL unleashes
349 the four-helix bundle domain to induce membrane localization and
350 necroptotic cell death. *Proc Natl Acad Sci U S A* **111**, 15072-15077
351 (2014).
352 13. H. Wang *et al.*, Mixed lineage kinase domain-like protein MLKL causes
353 necrotic membrane disruption upon phosphorylation by RIP3. *Mol Cell*
354 **54**, 133-146 (2014).
355 14. G. Quarato *et al.*, Sequential Engagement of Distinct MLKL
356 Phosphatidylinositol-Binding Sites Executes Necroptosis. *Mol Cell* **61**,
357 589-601 (2016).
358 15. A. Bendahmane, K. Kanyuka, D. C. Baulcombe, The Rx gene from
359 potato controls separate virus resistance and cell death responses.
360 *Plant Cell* **11**, 781-792 (1999).
361 16. N. S. Coll *et al.*, Arabidopsis type I metacaspases control cell death.
362 *Science* **330**, 1393-1397 (2010).
363 17. J. S. Pearson, J. M. Murphy, Down the rabbit hole: Is necroptosis truly
364 an innate response to infection? *Cell Microbiol* **19**, (2017).

365 18. G. Manning, D. B. Whyte, R. Martinez, T. Hunter, S. Sudarsanam, The
366 protein kinase complement of the human genome. *Science* **298**, 1912-
367 1934 (2002).
368 19. W. Wang, Y. Wen, R. Berkey, S. Xiao, Specific targeting of the
369 Arabidopsis resistance protein RPW8.2 to the interfacial membrane
370 encasing the fungal Haustorium renders broad-spectrum resistance to
371 powdery mildew. *Plant Cell* **21**, 2898-2913 (2009).
372 20. E. A. van der Biezen, C. T. Freddie, K. Kahn, J. E. Parker, J. D. Jones,
373 Arabidopsis RPP4 is a member of the RPP5 multigene family of TIR-
374 NB-LRR genes and confers downy mildew resistance through multiple
375 signalling components. *Plant J* **29**, 439-451 (2002).
376 21. F. Jacob *et al.*, A dominant-interfering camta3 mutation compromises
377 primary transcriptional outputs mediated by both cell surface and
378 intracellular immune receptors in Arabidopsis thaliana. *New Phytol* **217**,
379 1667-1680 (2018).
380 22. J. M. Murphy *et al.*, The pseudokinase MLKL mediates necroptosis via
381 a molecular switch mechanism. *Immunity* **39**, 443-453 (2013).
382 23. M. C. Tanzer *et al.*, Evolutionary divergence of the necroptosis effector
383 MLKL. *Cell Death Differ* **23**, 1185-1197 (2016).
384 24. J. Marc *et al.*, A GFP-MAP4 reporter gene for visualizing cortical
385 microtubule rearrangements in living epidermal cells. *Plant Cell* **10**,
386 1927-1940 (1998).
387 25. A. R. Bentham, R. Zdrzalek, J. C. De la Concepcion, M. J. Banfield,
388 Uncoiling CNLs: Structure/Function Approaches to Understanding CC
389 Domain Function in Plant NLRs. *Plant Cell Physiol* **59**, 2398-2408
390 (2018).
391 26. C. Barragan *et al.*, RPW8/HR Repeats Predict NLR-dependent Hybrid
392 Performance. *bioRxiv*, 559864 (2019).
393 27. L. M. Jubic, S. Saile, O. J. Furzer, F. El Kasmi, J. L. Dangl, Help
394 wanted: helper NLRs and plant immune responses. *Curr Opin Plant*
395 *Biol* **50**, 82-94 (2019).
396 28. S. M. Collier, L. P. Hamel, P. Moffett, Cell death mediated by the N-
397 terminal domains of a unique and highly conserved class of NB-LRR
398 protein. *Mol Plant Microbe Interact* **24**, 918-931 (2011).
399 29. V. Bonardi *et al.*, Expanded functions for a family of plant intracellular
400 immune receptors beyond specific recognition of pathogen effectors.
401 *Proc Natl Acad Sci U S A* **108**, 16463-16468 (2011).

402

402 **Methods**

403 **Plant material and growth conditions**

404 *The Arabidopsis thaliana* (L.) Heynh. ecotype Columbia (Col-0) was *used in*
405 *this study. The T-DNA insertional mutants(1, 2) (SALK_041569c (AtMLKL1),*
406 *SALK_124412c (AtMLKL2) and GABI_491E02 (AtMLKL3) were obtained*
407 *from the Nottingham Arabidopsis Stock Centre (NASC).* Double and triple
408 mutants of *Atmlkl* were generated by crossing the T-DNA insertion lines. A
409 segregant line derived from the cross between the *Atmlkl1* and *Atmlkl3*
410 mutants were used as a wild-type line in addition to Col-0 wild-type. Each
411 genotype was confirmed by PCR. The *eds1-2* mutant was described
412 previously (*3*).

413 *The transgenic lines expressing AtMLKL1 variants or AtMLKL2 fused to a*
414 *monomeric green fluorescence protein* were established in *Atmlkl1* and
415 *Atmlkl2* mutant backgrounds, respectively. Genomic fragments including
416 coding region and native *cis*-regulatory sequence were amplified by PCR from
417 Col-0 genomic DNA and cloned into pENTR/D-TOPO (Thermo Fisher
418 Scientific, Waltham, MA, USA). The phosphomimetic substitutions were
419 introduced using the QuikChange Lightning site-directed mutagenesis kit
420 (Agilent Technologies, Santa Clara, CA, USA). Resulting entry vectors were
421 transferred into pGWB550(*4*) using LR clonase II (Thermo Fisher Scientific).
422 Plants were transformed by the floral dip method (*5*) with *Agrobacterium*
423 *tumefaciens* strain GV3101 harbouring pMP90RK (*6*). Plant growth conditions
424 were described previously (*7*). Primer sequences for genotyping and plasmid
425 construction are listed in Table S3.

426

427 **Sequence analysis of plant and animal MLKLs**

428 Sequence similarity within the animal and plant families was established by
429 the generalized profile method (*8*). Sequences were aligned by the L-INS-I
430 method of the MAFFT alignment software (*9*), followed by minor manual
431 editing of ambiguously aligned regions. Sequence similarity between the
432 animal and plant MLKL families was established by Hidden Markov Model
433 (HMM)-to-HMM comparison using the HHSEARCH package (*10*). The 99,696
434 orthogroups (OGs) among 52 plant species have been established recently
435 (*11*). An OG containing *At*MLKLs was used for the neighbor-net analysis of
436 codon-aligned nucleotide sequence as descried previously (*12*). The
437 sequence from the papaya genome was excluded in this study.

438 **Protein expression and purification**

439 Full length *At*MLKL3 (residues 1-701) with an engineered C-terminal 6×His
440 tag was generated by standard PCR-based cloning strategy and its identity
441 was confirmed by sequencing. The protein was expressed in sf21 insect cells
442 using the vector pFastBac 1 (Invitrogen). One litre of cells (2.5×10^6 cells ml^{-1},
443 medium from Expression Sysems) was infected with 20 ml baculovirus at
444 28°C. After growth at 28°C for 48 hours, the cells were harvested, re-
445 suspended in the buffer containing 50 mM Tris-HCl pH 8.0 and 300 mM NaCl,
446 and lysed by sonication. The soluble fraction was purified from the cell lysate
447 using Ni2+-nitrilotriacetate affinity resin (Ni-NTA, Qiagen). The protein was
448 then further purified by further purified by gel filtration (Superose 6, 10/30; GE
449 Healthcare). For cryo-EM investigation, the purified protein was concentrated
450 to about 0.3 mg/mL in buffer containing 50 mM Tris-HCl pH 8.0, 300 mM NaCl
451 and 3 mM DTT.

452 The construct of full length *At*MLKL2 (residues 1-711) with N-terminal GST
453 tag was cloned into the pGEX-6P-1 vector (GE Healthcare), and was
454 expressed in *Escherichia coli* strain BL21(DE3; Novagen) at 16 °C. After
455 isopropyl-β-D-thiogalactopyranoside (IPTG; Sigma) induction for 12 h, cells
456 were harvested and re-suspended in buffer containing 50 mM Tris-HCl pH 8.0
457 and 300 mM NaCl, and lysed by sonication. The soluble fraction was purified
458 from the cell lysate using Glutathione Sepharose 4B beads (Invitrogen). The
459 proteins were then digested with PreScission protease (GE Healthcare) to
460 remove the GST tag and further purified by gel filtration (Superose 6, 10/30;
461 GE Healthcare). For cryo-EM investigation, the purified protein was
462 concentrated to about 0.3 mg/mL in buffer containing 50 mM Tris-HCl pH 8.0,
463 300 mM NaCl and 3 mM DTT.

464 **Cryo-EM sample preparation and data collection**

465 For cryo-EM analysis, an aliquot of 3.5 µl *At*MLKL2 or *At*MLKL3 protein was
466 applied to a holey carbon grids (Quantifoil Cu 1.2/1.3, 200 mesh) glow-
467 discharged (Harrick Plasma) with a middle force for 30 s after evaluating for 2
468 min. The grids were blotted by a pair of 55 mm filter papers (TED PELLA,
469 INC.) for 3-3.5 s at 8 °C with 100% humidity and flash-frozen in liquid ethane
470 using a FEI Vitrobot Marked IV. Cryo-EM data were collected on Titan Krios
471 electron microscope operated at 300 kV and a Gatan K2 Summit direct
472 electron detection camera (Gatan) using eTas. Micrographs were recorded in
473 super-resolution mode at a nominal magnification of 22500 ×, resulting in a
474 physical pixel size of 1.30654 Å per pixel. Defocus values varied from -1.7 µm
475 to -2.3 µm for data set. The dose rate was 10.6 electron per pixel per second.

476 Exposures of 8.0 s were dose-fractionated into 32 sub-frames, leading to a
477 total accumulated dose of 50 electrons per Å2. In total, two batches of data
478 were collected, one for *At*MLKL3 and another for *At*MLKL2.

479 **Image processing and 3D reconstruction**

480 A total of 1,434 and 1,828 raw images stacks of *At*MLKL3 and *At*MLKL2
481 acquired under super-resolution mode, were 2x binned processed using
482 MotionCor2 (*13*), generating aligned, dose-weighted and summed
483 micrographs in a pixel size of 1.30654 Å per pixel. CTFFIND4 (*14*) was used
484 to estimate the contrast transfer function (CTF) parameters. After the removal
485 of bad micrographs via the evaluation of CTF parameters, remaining images
486 were processed in RELION (*15*). Approximate 2,000 particles were manually
487 picked and 2D-classified to generate templates for auto-picking. 983,779 and
488 1,135,463 autopicked particles for *At*MLKL3 and *At*MLKL2 respectively were
489 then used for reference-free 2D classification, to remove contaminants and
490 bad particles. The left good particles were subjected to 3D classification using
491 initial 3D reference model obtained by *ab initio* calculation from Relion3.0.
492 Particles from good classes that possess density map with better overall
493 structure features were selected for the 3D refinement. The final 3D
494 refinement using D2 symmetry resulted in reconstructions of *At*MLKL3 and
495 *At*MLKL2 tetramer at resolution of 3.4 Å and 4.1 Å, the resolutions were
496 determined by gold-standard Fourier shell correlation. Local resolution
497 distribution was evaluated using Relion.

498

499

500 **Model building and refinement**

501 EM density map of *At*MLKL3 was used to build the model de novo, as the
502 overall resolution of map density was efficient to display side chains. The
503 model of *At*MLKL3 was manually built into the density in COOT(*16*), and was
504 refined against the EM map by PHENIX(*17*) in real space with secondary
505 structure and geometry restraints. The refined *At*MLKL3 model was docked
506 into the density of *At*MLKL2. The sequence of the docked *At*MLKL3 model
507 was changed to that of *At*MLKL2 under COOT and the *At*MLKL2 model with
508 corrected sequence was subjected to refinement by PHENIX. The C-terminal
509 serine-rich region of *At*MLKL2 or *At*MLKL3 is much less well defined in the
510 density and is not included in the models. Final model of *At*MLKL3 and
511 *At*MLKL2 was validated using MolProbity and EMRinger in PHENIX package.
512 The structures of human MLKL (*18*) and mouse MLKL (*19*) were used for the
513 superposition of the HeLo domains as shown in Fig. 2D.Table S2 summarized
514 the model statistics.

515 **RNA sequencing**

516 Total mRNA from leaves was obtained at 48 hours after challenge with
517 conidia of *Golovinomyces orontii* using the RNeasy plant mini kit (Qiagen).
518 RNA sequencing (RNA-Seq) libraries were prepared by the Max Planck
519 Genome Centre Cologne (Cologne, Germany) using the Illumina TruSeq
520 stranded RNA sample preparation kit (Illumina). The resulting libraries were
521 subjected to 150-bp single-end sequencing using the Illumina HiSeq3000
522 (Illumina). Mapping of sequenced reads onto the *Arabidopsis thaliana* gene
523 model (TAIR10), principal component analysis, and differential gene
524 expression analysis were performed in the CLC Genomics Workbench

525 (Qiagen, ver. 10.1.2) using the tool 'RNA-Seq with the default parameter
526 setting. The data derived from Col-0 and WT were pooled as data of wild-type
527 lines in the analysis. The heat map of 93 genes differentially expressed
528 between wild type lines and *Atmlkl* mutants (|log2FC|>1 and false discovery
529 rate (FDR) < 0.05) were generated using the R package (ver. 1.08) with the
530 pheatmap function. Gene ontology enrichment analysis was performed using
531 the PANTHER classification system (http://pantherdb.org/) with default
532 settings for *Arabidopsis thaliana*. The RNA-Seq data generated in this study
533 have been deposited in the Gene Expression Omnibus (GEO) database
534 under accession number GSE129011.

535

536 **Transient gene expression in *Arabidopsis* protoplasts**

537 Isolation, transfection and luciferase activity measurement of Arabidopsis
538 protoplasts were performed as described previously (*20*). Protoplasts were
539 isolated from the leaves of two-week-old *Arabidopsis* plants grown in liquid 1 x
540 Murashige and Skoog medium. Coding sequences (CDS) of *AtMLKL1* and
541 *AtMLKL2* without stop codons were initially cloned into pENTR/D-TOPO
542 (Thermo Fisher Scientific). The CDS of *AtMLKL3* without a stop codon was
543 chemically synthesized and cloned into pENTR221 (Thermo Fisher Scientific).
544 Two synonymous substitutions (G1371T and A1413G) were introduced into
545 *AtMLKL3* CDS to remove restriction sites that hamper the DNA synthesis.
546 Entry clones were transferred into the gateway cloning-compatible pAMPAT-
547 GW-mYFP, pAMPAT-GW-3xHA, or pAMPAT-GW expression vectors (*21*),
548 which are derivatives of pAMPAT-MCS (accession number: AY436765).
549 Primers sequences of for plasmid construction are listed in Table S3. pENTR-

550 tagRFP-T-Lifeact (*22*) was transferred into pAMPAT-GW. The expression
551 vectors for *Hv*MLA(1-160aa), MAP4 and Tub6 were described previously (*21,*
552 *23, 24*).

553 **Protoplast viability assay**

554 Following protoplast transfection and regeneration, Evans blue dye dissolved
555 in water was added to the samples to a final concentration of 0.04% (w/v).
556 The stained cells were examined under a standard microscope. For
557 luciferase-based viability assay luciferase and *At*MLKL expression constructs
558 were co-transfected into protoplasts and luciferase activity was measured as
559 a proxy of cell viability.

560

561 **Induced oligomerization**

562 Two domains of FKBP (F36V) tagged with HA without N-myristoylation signal
563 were PCR amplified from pC4M-FV2E plasmid (ARIAD, Cambridge, MA,
564 USA). *Nco*I and *Hind*III restriction sites were added to the 5' end of forward
565 and reverse primers, respectively. The digested PCR fragment with *Nco*I and
566 *Hind*III were ligated into the same restriction sites present between the attR2
567 and the terminator sequences of pAMPAT-GW expression vector. The
568 resulting vector is named pAMPAT-GW-FV2E-HA. Coding regions
569 corresponding to the N- and C-terminal luciferase fragments (nLUC and
570 cLUC) were PCR amplified from nLUC and cLUC expression vectors (*25*) and
571 cloned into pENTR/D-TOPO. Respective entry clones were transferred into
572 pAMPAT-GW-FV2E-HA. B/B homodimerizer (also known as AP20187 ligand)
573 were purchased from TakaraBio, Japan. After transfection, protoplasts in

574 incubation buffer (i.e. WI solution (*26*)) were separated into two tubes and
575 added the same amount of incubation buffer supplemented with B/B
576 homodimerizer (250 nM at the final concentration) or ethanol as solvent
577 control. Primer sequences for the plasmid construction are listed in Table S2.
578 We were able to reconstitute luciferase activity of co-expressed N- and C-
579 terminal halves of luciferase fused to 2xDmrB domains in a ligand-specific
580 manner (Fig. S8b) and the ligand itself did not affect the luciferase reporter
581 assay in protoplasts (Fig. S8c).

582 **Pathogen infection assay**

583 The *G. orontii* infection assay was performed as described previously (*27*). *G.*
584 *orontii* DNA was quantified by qPCR at indicated time points after inoculation
585 of conidia and normalised using the amount of plant specific gene
586 (AT3G21215). The *Hpa* infection assay was performed as previously
587 described (*28*). Lactophenol-trypan blue staining was described previously
588 (*29*). The *B. cinerea* strain B05.10 was used in this study. Droplet inoculation
589 of six-week-old plants was performed as described previously (*30*), except
590 that 2 µl of the spore solution were used on each side of the leaf and two
591 leaves of similar age were used per plant. *B. cinerea* DNA was quantified by
592 qPCR as previously described (*31*). *Pseudomonas syringae* pv. *tomato* (*Pst*)
593 DC3000 and *Pst* DC3000 expressing *AvrRpt2* or *AvrRpm1* were used in this
594 study. *Pst* growth assays and ion leakage measurement following bacterial
595 infiltration were performed as described previously (*7*).

596

597

598 **Immunoblot assays**

599 Primary antibodies were monoclonal antibodies from mouse: α-GFP (JL-8,
600 1:5000, Takara, Shiga, Japan) or rat: α-HA (3F10, 1:1000, Sigma-Aldrich, St.
601 Louis, MO, USA). Goat α-mouse IgG-HRP (1:10000, Santa Cruz
602 Biotechnology, Dallas, TX, USA) or goat α-rat IgG-HRP (1:10000, Sigma-
603 Aldrich) were used as secondary antibodies. The detailed procedure is
604 described in (*7*).

605

606 **Biolistic transient gene expression**

607 Biolistic delivery of plasmid DNA into the abaxial epidermis of leaves was
608 essentially performed as described previously (*32*). Leaves were detached
609 immediately before bombardment and the bombarded leaves were transferred
610 to 1% agar plates supplemented with 85 μM benzimidazole and incubated at
611 20°C for 15 h before confocal microscopy.

612

613 **Confocal microscopy**

614 Transfected protoplasts in a chamber slide (Nunc Lab-Tek, Thermo Fisher
615 Scientific) with incubation buffer (i.e. WI solution, (*26*)) or 2-5 mm leaf discs
616 prepared form rosette leave of 4-5-week-old plants were observed under a
617 confocal microscope (LSM880, Carl Zeiss) equipped with a 40X water-
618 immersion and a 63X oil-immersion objective. Lambda stack images were
619 obtained for spectral imaging. Images were analyzed and processed with ZEN
620 Software (Carl Zeiss) and ImageJ (NIH). In Fig. 4E, confocal images were
621 acquired over time (for wild type, 124 seconds; for S393D, 194 seconds; for

622 S395D, 166 seconds) and used for maximum intensity projection (bottom
623 panels). Representative single frame images are shown (top panels).

624

Supplemental data

Supplemental Fig. 1: 3D reconstruction of *At*MLKL3 tetramer

A, Representative cryo-EM image of *At*MLKL3 tetramer. Representative particles are indicated with black circles.
B, Representative top and side views of 2D class averages of *At*MLKL3 tetramer.
C, Fourier shell correlation (FSC) curves at 0.5 and 0.143 of the 3D reconstruction of *At*MLKL3 tetramer.
D, Flowchart representing cryo-EM data processing and 3D reconstruction of *At*MLKL3 tetramer.

Supplemental Fig. 2: Purification and 3D reconstruction of *At*MLKL2 tetramer

A, Top: Gel filtration profile of *At*MLKL2 protein. Position of standard molecular weight is indicated by arrow. Bottom: Peak fractions in the top were verified by SDS-PAGE with Coomassie Blue staining.
B, Representative cryo-EM images of the *At*MLKL2 tetramer. Representative particles are indicated with black circles.
C, Representative top and side views of 2D class averages of *At*MLKL2 tetramer.
D, Fourier shell correlation (FSC) curves at 0.5 and 0.143 of the 3D reconstruction of *At*MLKL2 tetramer.
E, Flowchart representing cryo-EM data processing and 3D reconstruction of *At*MLKL2 tetramer.

Supplemental Fig. 3: Inter- and intra-domain interactions of *At*MLKL3 tetramer and structural comparison of the *At*MLKL2 and *At*MLKL3

A, Superposition of *At*MLKL2 (grey) and *At*MLKL3 (blue). RMSD between monomer of *At*MLKL2 and *At*MLKL3 :0.985.

B, The sequence of *At*MLKL3 model (blue) was docked into *At*MLKL2 map (gray).

C, Top: Cartoon representation of *At*MLKL3 monomer in two orientations. Subdomains of *At*MLKL3 are shown in different colors, the interacting regions between domains are highlighted with open frames. Bottom left: Detailed interactions of HeLo domain and pseudokinase domain for the red-framed region. Bottom right: Detailed interactions of HeLo domain and brace region for the blue-framed region.

D, Structural comparison of the monomer *At*MLKL2 (left), *At*MLKL3 (middle, PDB ID code 6KA4) and *m*MLKL (right, PDB ID code 4BTF).

E, Top left: Cartoon showing HeLo domain and brace region of *At*MLKL3 tetramer. Top right: Detailed interactions of HeLo domains for the green-

668 framed region. Bottom left: Detailed C-terminal interactions of brace regions
669 for the blue-framed region. Bottom right: Detailed N-terminal interactions of
670 brace regions for the blue-framed region.
671
672 **Supplemental Fig. 4: *Atmlkl* mutants exhibit no obvious growth defect.**

673 **A,** The Arabidopsis *MLKL* genes and T-DNA insertion sites of the *Atmlkl*
674 mutants. White and black boxes indicate non-coding and coding exons,
675 respectively. A gene model for *AtMLKL3* was deduced from other plant *MLKL*
676 structures.

677 **B**, Representative images of four-week-old plants of Col-0, wild type*, single
678 mutants of *Atmlkl1*, *Atmlkl2*, *Atmlkl3*, double mutants *Atmlkl1 2*, *Atmlkl1 3*,
679 *Atmlkl2 3*, and the triple mutant *Atmlkl1 2 3*. *The wild type is a segregant line
680 derived from the cross between *Atmlkl1* and *Atmlkl3*. The plants were initially
681 grown on Murashige and Skoog-agar plates for two weeks and subsequently
682 transferred to Jiffy pots rehydrated in water with a fertilizer. Plants were grown
683 for an additional two weeks under short-day conditions.

684

685 **Supplemental Fig. 5: *Arabidopsis* MLKLs do not confer resistance to**
686 ***Botrytis cinerea* and *Pseudomonas syringae* DC3000.**

687 **A**, *Botrytis cinerea* DNA was quantified by qPCR at three days after spore
688 inoculation and normalized using the amount of plant specific gene (see
689 method). Amounts are presented relative to the corresponding Col-0 samples.
690 The wild type is a segregant line derived from the cross between *Atmlkl1* and
691 *Atmlkl3* (see Fig. S4). Data were obtained in three independent experiments
692 (n=3).

693 **B**, Log_{10}-transformed colony forming units of *Pseudomonas syringae* DC3000
694 per cm^2 of *A. thaliana* leaves at two days after pathogen infiltration. The *eds1*
695 mutant was used as a susceptible control. Data were obtained in three
696 independent experiments (n=3).

697 **C**, Log_{10}-transformed colony forming units of *P. syringae* DC3000 expressing
698 AvrRpt2 per cm^2 of *A. thaliana* leaves at three days after pathogen infiltration.
699 The *rpm1 rps2* mutant was used as a susceptible control. Data were obtained
700 in three independent experiments (n=3).

701 **D**, Ion leakage assay in *A. thaliana* leaves upon infiltration with *P. syringae*
702 DC3000 expressing *AvrRpm1*. Samples were collected 30 min post infiltration
703 with the bacterial suspension (OD600=0.1). The *rpm1 rps2* mutant was used
704 as a negative control. Data were obtained in three independent experiments
705 (n=3).

706 n.s. not significant.

707 **Supplemental Fig. 6: Heat map of 93 genes differentially expressed in**
708 ***Atmlkl123* in comparison to wild type.** The gene ontology (GO) term biotic
709 or abiotic stresses (GO:0006950, asterisks) was overrepresented in the down-
710 regulated transcripts in *Atmlkl123* compared to wild type lines. Mock- and

711 pathogen-challenged leaves were collected at 48 hours post *G. orontii*
712 inoculation. *WT is a segregant line derived from the cross between *Atmlkl1*
713 and *Atmlkl3*.

714 **Supplemental Fig. 7: *At*MLKLs are capable of eliciting cell death in**
715 ***Arabidopsis* mesophyll protoplasts.**

716 **A**, C-terminally HA-tagged and **B**, C-terminally mYFP-tagged *At*MLKLs were
717 expressed under the constitutive cauliflower mosaic virus 35S promoter.
718 Expression constructs for *At*MLKLs were transfected into protoplasts and cells
719 were stained with Evans blue at 16 hours post transfection. Unstained cells
720 (Evans blue-negative cells) were counted as living cells. For **B**, The N-
721 terminal signalling region of barley NLR protein (*Hv*MLA$_{1-160}$: (*7*) was used as
722 a positive control. Data were obtained in three independent transfections
723 (n=3) and different letters indicate statistically significant differences (Tukey
724 HSD, $p < 0.01$).

725 **C**. Phosphomimetic substitutions in *At*MLKL2 or *At*MLKL3 do not alter cell
726 death in *Arabidopsis* mesophyll protoplasts.

727 Expression constructs for luciferase and each of the *At*MLKL variants were
728 co-transfected into protoplasts and luciferase activity was measured as a
729 proxy for cell viability at 16 hours post transfection. The positions of serine-to-
730 aspartate substitutions are indicated in Fig. 1B. The C-terminally HA-tagged
731 variants were expressed under the 35S promoter. Data were obtained in three
732 independent transfections (n=3). n.s. not significant.

733 **D**, Western blot analysis of expression of C-terminally HA-tagged *At*MLKLs in
734 *Arabidopsis* mesophyll protoplasts. Total protein extracts were collected at
735 seven hours post transfection. Samples that were transfected with the
736 corresponding empty vector or the expression construct for *At*MLKL2-mYFP
737 were used as negative control.

738

739 **Supplemental Fig. 8: Genetic complementation of the *Atmlkl1* mutant.**

740 **A,** Macroscopic phenotype of transgenic *Arabidopsis* lines expressing wild-
741 type or phosphomimetic variants of *At*MLKL1-GFP under the native *cis*-
742 regulatory sequence in in *Atmlkl1* in response to *G. orontii*. Plants were
743 photographed seven days after pathogen challenge.

744 **B,** Western blot analysis of the C-terminally GFP-tagged *At*MLKL1 variants in
745 the stable transgenic lines. Total protein extracts were collected from two-
746 week-old plants of the transgenic lines grown on sterile Murashige and Skoog
747 solid media.

748

749 **Supplemental Fig. 9: Genetic complementation of the *Atmlkl2* mutant.**

750 **A,** Macroscopic phenotype of transgenic *Arabidopsis* lines expressing
751 *At*MLKL2-GFP under the native *cis*-regulatory sequence in *Atmlkl2*. Four-

752 week-old plants were inoculated with *G. orontii* spores and plants were
753 photographed at 14 days after pathogen challenge.

754 **B**, Western blot analysis of C-terminally GFP-tagged *At*MLKL2. Total protein
755 extracts were collected from two-week-old plants of the transgenic lines grown
756 on sterile Murashige and Skoog solid media.

757 The asterisk and arrow indicate non-specific and specific bands, respectively.

758 **C,** Quantification of *G. orontii* DNA in infected leaves. Four-week-old plants
759 were inoculated with spores of the powdery mildew and plants were examined
760 at 14 days after the pathogen challenge. Fungal DNA was quantified by qPCR
761 and normalised using the amount of plant specific gene (AT3G21215). The
762 relative amounts to corresponding Col-0 wild-type samples were presented.
763 Experiments were repeated three times (n=3) and the asterisk indicates a
764 statistically significant difference (Tukey HSD, $p < 0.05$).

765

766 **Supplemental Fig. 10: N-terminal domains of *At*MLKL1 and 3 were**
767 **sufficient to elicit cell death and their enforced oligomerization**
768 **potentiated the activities.**

769 **A,** Schematic of chemically induced oligomerization. AP20187 (Dimerizer), a
770 synthetic cell-permeable ligand, induces homodimerization of fusion proteins
771 containing the DmrB domain. Dimerizer–dependent oligomerization is
772 facilitated by a tandem fusion of DmrB domains.

773 **B**, Dimerizer–induced reconstitution of luciferase activity of the N- or C-
774 terminal halves of luciferase fused with 2 x DmrB domains. Data were
775 obtained with eight independent transfections (n=8). Luciferase activity was
776 measured at 16 hours post transfection. The luciferase activity was
777 statistically higher in the presence of dimerizer (one sample *t*-test, $p < 0.01$).

778 **C,** Dimerizer does not influence the luciferase reporter assay. Data were
779 obtained with seven independent transfections (n=7). Luciferase activity was
780 measured at 16 hours post transfection. No statistically significant differences
781 were detected (one sample *t*-test).

782 **D**, HeLo domain plus brace region of *At*MLKL1 and *At*MLKL3 were sufficient
783 to elicit cell death and their enforced oligomerization potentiated the activities.
784 Expression constructs for luciferase and each of the *At*MLKL fusion proteins
785 indicated in the figure were co-transfected into protoplasts and luciferase
786 activity was measured as a proxy of cell viability at 16 hours post transfection.
787 Relative luciferase activities compared to those of the empty vector control
788 with dimerizer were plotted. Data were obtained with eight independent
789 transfections (n=9). Asterisks indicate statistically significant differences
790 (Tukey HSD, $p < 0.01$)

791 **E,** Western blot analysis of the HeLo domain plus brace region constructs
792 expressed in *Arabidopsis* mesophyll protoplasts. The fusion proteins were
793 expressed as C-terminally HA-tagged proteins. Total protein extracts were
794 collected at seven hours post-transfection.

795 **B-E,** Mesophyll protoplasts were prepared from the triple mutant *Atmlkl123*
796 and AP20187 (Dimerizer) was added after transfection (see method).

797

798 **Supplemental Fig. 11: Subcellular localization of *At*MLKLs in protoplasts.**

799 **A,** Subcellular localization of *At*MLKLs in *Arabidopsis* mesophyll protoplasts.
800 The C-terminally monomeric YFP (mYFP)-tagged variants were expressed
801 under the 35S promoter. Representative confocal images were taken at ten
802 hours post transfection. Scale bars = 10 μm.

803 **B**, Co-expression of *At*MLKL1 and cytoskeleton markers in *Arabidopsis*
804 mesophyll protoplasts. Co-expression of *At*MLKL1-mYFP and mcherry-MAP4
805 (microtubule marker: (*33*) top panels), or tagRFP-T-Lifeact (Actin marker: (*34*)
806 middle panels). Representative confocal images were taken at 10 hours post
807 transfection. Scale bars = 10 μm.

808 **C**, The filamentous structures of *At*MLKL1-mYFP were undetectable at 5
809 minutes after application of 5 uM of the microtubule inhibitor, oryzalin.
810 Representative confocal image was taken at 10 hours post transfection.
811 Scale bar = 10 μm.

812 **Supplemental Fig. 12: Confocal images of an epidermal cell that was**
813 **infected by *G. orontii*.** The maximum intensity projection was obtained from
814 confocal Z-stack images and the autofluorescence of fungal structures were
815 discriminated from *At*MLKL1-GFP signals by spectral imaging. Arrowheads
816 indicate filamentous structures associated with *At*MLKL1-GFP. C; cytoplasm,
817 Ha: haustorium, E, haustorial encasement. Scale bar = 5 μm.

818 **Supplemental Fig. 13: Cortical microtubule arrays in abaxial leaf**
819 **epidermal cells of *transgenic A. thaliana lines expressing***
820 **phosphomimetic and wild type variants of *At*MLKL1.** Representative
821 images were obtained one day after biolistic delivery of the expression
822 construct for the *At*ubiqutin10 promoter driven by mCherry-TUB6 (microtubule
823 marker (*24*)) into the indicated transgenic lines. Scale bars = 10 μm.

824

825 **Supplemental movie 1**

826 Dynamics of *At*MLKL1(wild-type)-GFP in a non-pathogen-challenged abaxial
827 leaf epidermal cell. The corresponding projection image is shown in Fig. 4E.
828 The white circle indicates a GFP signal proximal to the PM (see Fig. 4D) and
829 which was less mobile compared to other signals.

830

831 **Supplemental movie 2**

832 Dynamics of *At*MLKL1(S393D)-GFP in a non-pathogen-challenged abaxial
833 leaf epidermal cell. The corresponding projection image is shown in Fig. 4E.

834 The white circle indicates a GFP signal proximal to the PM (see Fig. 4D) and
835 which was less mobile compared to other signals.

836

837 **Supplemental movie 3**

838 Dynamics of *At*MLKL1(S395D)-GFP in a non-pathogen-challenged abaxial
839 leaf epidermal cell. The corresponding projection image is shown in Fig. 4E.
840 The white circle indicates a GFP signal proximal to the PM (see Fig. 4D) and
841 which was less mobile compared to other signals.

842

843 **Supplemental file 1**

844 108 coding sequences (CDS) of plant *MLKLs* belong to the same orthogroups
845 (*11*). A CDS derived from *Arabidopsis halleri* is incomplete due to the
846 ambiguous assembly of the corresponding genomic region.

847

847

Table S1. Number of MLKL-like genes in plant genomes

Plant species	NCBI Taxonomy ID	Family	Number of *MLKL*-like genes
Coccomyxa subellipsoidea	248742	Coccomyxaceae	0
Ostreococcus lucimarinus	242159	Bathycoccaceae	0
Volvox carteri	3067	Volvocaceae	0
Physcomitrella patens	3218	Funariaceae	0
Selaginella moellendorffii	88036	Selaginellaceae	0
Actinidia chinensis	3625	Actinidiaceae	3
Amborella trichopoda	13333	Amborellaceae	1
Spirodela polyrhiza	29656	Araceae	2
Phoenix dactylifera	42345	Arecaceae	3
Arabidopsis halleri	81970	Brassicaceae	2
Arabidopsis lyrata	59689	Brassicaceae	3
Arabidopsis thaliana	3702	Brassicaceae	2
Brassica oleracea	3712	Brassicaceae	3
Brassica rapa	3711	Brassicaceae	2
Boechera stricta	72658	Brassicaceae	3
Capsella grandiflora	264402	Brassicaceae	3
Capsella rubella	81985	Brassicaceae	3
Eutrema salsugineum	72664	Brassicaceae	4
Schrenkiella parvula	98039	Brassicaceae	3
Beta vulgaris	161934	Chenopodiaceae	2
Cucumis sativus	3659	Cucurbitaceae	2
Ricinus communis	3988	Euphorbiaceae	2
Arachis ipaensis	130454	Fabaceae	2
Medicago truncatula	3880	Fabaceae	2
Phaseolus vulgaris	3885	Fabaceae	2
Linum usitatissimum	4006	Linaceae	4
Gossypium raimondii	29730	Malvaceae	3
Theobroma cacao	3641	Malvaceae	2
Musa acuminata	4641	Musaceae	4
Erythranthe guttata	4155	Phrymaceae	2
Pinus taeda	3352	Pinaceae	1
Brachypodium distachyon	15368	Poaceae	2
Oryza sativa	4530	Poaceae	2
Sorghum bicolor	4558	Poaceae	2
Setaria italica	4555	Poaceae	2
Zea mays	4577	Poaceae	2
Aquilegia coerulea	218851	Ranunculaceae	1
Fragaria vesca	57918	Rosaceae	2

Malus domestica	3750	Rosaceae	5
Prunus persica	3760	Rosaceae	2
Coffea canephora	49390	Rubiaceae	2
Citrus clementina	85681	Rutaceae	2
Citrus sinensis	2711	Rutaceae	2
Populus trichocarpa	3694	Salicaceae	2
Capsicum annuum	4072	Solanaceae	3
Solanum melongena	4111	Solanaceae	3
Solanum lycopersicum	4081	Solanaceae	3
Solanum tuberosum	4113	Solanaceae	3
Vitis vinifera	29760	Vitaceae	2

849 **Table S2. Cryo-EM statistics and model refinement for *At*MLKL tetramer**

	*At*MLKL3 tetramer	*At*MLKL2 tetramer
Data collection and processing		
Microscope	FEI Titan Krios	FEI Titan Krios
Detector	Gatan K2 Summit	Gatan K2 Summit
Voltage(kV)	300	300
Magnification	22500x	22500x
Pixel size (Å)	1.30654	1.30654
Total electron dose (e^-/Å^2)	50	50
Defocus range (μm)	-1.5 ~ -2.3	-1.6~-2.2
Micrographs collected	1,434	1,828
Reconstruction		
Total extraced particles	983,779	1,527,009
Number of particles used for 3D reconstruction	629,287	796,901
Number of particles used for refinement	123,472	154,008
Symmetry	D2	D2
Resolution (Å) 0.143 after refinement	3.84	4.51
Resolution (Å) 0.143 after post-processing	3.39	4.08
Map sharpening B-factor (Å^2)	-152	-222.79
Refinement		
Estimated Resolution (Å)	3.4	4.1
Model composition		
Number of protein atoms	16584	14238
Number of ligand atoms	0	0
MapCC (mask/box)	0.83/0.79	0.81/0.81
Rwork/Rfree (%)	34.35/34.35	39.4/39.4
R.M.S deviations		
Bonds lengths (Å)	0.011	0.010
Bonds angles (°)	0.941	0.797
Validation		
MolProbity overall score	2.22	2.56
All-atom clashscore	15.96	18.07
Rotamer outliers (%)	0.67	1.57
C-beta deviations	0.0	0.0
EMRinger score	1.56	1.42
Ramachandran plot statistics		
Preferred (%)	91.27	85.27
Allowed (%)	8.33	14.31
Outlier (%)	0.40	0.42

850

851

852

853 **Table S3 Primer pairs used in this study.**

Forward primer	Sequence 5′-3′	Reverse primer	Sequence 5′-3′	Use, comments
SALK_041569c_RP	GAGAGACAGCGAAAACCTGTG	SALK_041569c_LP	CTTCTCTTGCAATGCCTCAAC	Genotyping of the wild type allele of *AtMLKL1*
SALK_041569c_RP	GAGAGACAGCGAAAACCTGTG	LBb1.3	ATTTTGCCGATTTCGGAAC	Genotyping of the mutant allele of *AtMLKL1*
SALK_124412c_RP AT5G41730	TCAGCTTAGCTTTCAACACGG	SALK_124412c_LP AT5G41730	GAAGATACTCCATCCCCCTTG	Genotyping of the wild type allele of *AtMLKL2*
SALK_124412c_RP AT5G41730	TCAGCTTAGCTTTCAACACGG	LBb1.3	ATTTTGCCGATTTCGGAAC	Genotyping of the mutant allele of *AtMLKL2*
GABI_491E02_RP	TACACGAAGCCCATTCACTTC	GABI_491E02_LP	TATTACCTCTGCGGATTCACG	Genotyping of the wild type allele of *AtMLKL3*
GABI_o3144/35St	GTGGATTGATGTGATATCTCC	GABI_491E02_LP	TATTACCTCTGCGGATTCACG	Genotyping of the mutant allele of *AtMLKL3*
AT1g64300-Fw1	CACCATGGAGCAATTCAGGCAAATCGGAGAGGTT	AT1g64300-Rv1	TGTAAGCTCAGAGTCTGAAGCAGGACCAGTTA	D-topo cloning of *At*MLKL1 cDNA without STOP codon
AT5G41730-Fw1	CACCATGGAGCAATTCAGACAAATCGGAGAAGTTCTT	AT5G41730-Rv1	AGTAAGCTCAGAGTCTGAAGCATGACCAGTCTGTT	D-topo cloning of *At*MLKL2 cDNA without STOP codon
D-topo-*At*MLKL3-f	CACCATGGATCAATTTCGAGAGATAGGAGAGGTATT	D-topo-*At*MLKL3-r_without_stop	GGAAAGCTCAGAGTCAGAGGCATGT	D-topo cloning of *At*MLKL3 cDNA without STOP codon
*At*MLKL1(S393D)-f	CCTCAGTTAAGAATCAGGATTTTTCTCGGGCTTCC	*At*MLKL1(S393D)-r	GGAAGCCCGAGAAAAATCCTGATTCTTAACTGAGG	Site-directed mutagenesis to obtain *At*MLKL1(S393D) variant
*At*MLKL1(S395D)-f	GTTAAGAATCAGTCTTTTGATCGGGCTTCCTCTAGAC	*At*MLKL1(S395D)-r	GTCTAGAGGAAGCCCGATCAAAAGACTGATTCTTAAC	Site-directed mutagenesis to obtain *At*MLKL1(S395D) variant
AT5G41730_(S394D)-f	GTCGTTAAAGCGCAGGATTCCTCGAAACCAG	AT5G41730_(S394D)-r	CTGGTTTCGAGGAATCCTGCGCTTTAACGAC	Site-directed mutagenesis to obtain *At*MLKL2(S394D) variant
AT5G41730_(S395D)-f	CGTTAAAGCGCAGTCTGATTCGAAACCAGGCACTCC	AT5G41730_(S395D)-r	GGAGTGCCTGGTTTCGAATCAGACTGCGCTTTAACG	Site-directed mutagenesis to obtain *At*MLKL2(S395D) variant
*At*MLKL3(S392D)-f	GTTGAATTCTGTCAAGGGATTCGATAGTAAAAGTGCTTCTTTGACG	*At*MLKL3(S392D)-r	CGTCAAAGAAGCACTTTTACTATCGAATCCCTTGACAGAATTCAAC	Site-directed mutagenesis to obtain *At*MLKL3(S392D) variant
*At*MLKL3(SS393D)-f	CTGTCAAGGGATTCTCTGATAAAAGTGCTTCTTTGAC	*At*MLKL3(S393D)-r	GTCAAAGAAGCACTTTTATCAGAGAATCCCTTGACAG	Site-directed mutagenesis to obtain *At*MLKL3(S393D) variant
Genomic of	CACCCCTTG	Genomic of	TGTAAGCT	D-topo cloning of genomic fragments

*At*3g21215-f	GAATCCACC CATACCACC AG	*At*3g21215-r	GAGGAGG AGGATGGT GATGA	qPCR quantification of the Arabidopsis DNA

854

855

856

856 **Supplemental References**

857 1. N. Kleinboelting, G. Huep, A. Kloetgen, P. Viehoever, B. Weisshaar,
858 GABI-Kat SimpleSearch: new features of the Arabidopsis thaliana T-
859 DNA mutant database. *Nucleic Acids Res* **40**, D1211-1215 (2012).
860 2. J. M. Alonso *et al.*, Genome-wide insertional mutagenesis of
861 Arabidopsis thaliana. *Science* **301**, 653-657 (2003).
862 3. M. Bartsch *et al.*, Salicylic acid-independent ENHANCED DISEASE
863 SUSCEPTIBILITY1 signaling in Arabidopsis immunity and cell death is
864 regulated by the monooxygenase FMO1 and the Nudix hydrolase
865 NUDT7. *Plant Cell* **18**, 1038-1051 (2006).
866 4. T. Nakagawa *et al.*, Improved Gateway binary vectors: high-
867 performance vectors for creation of fusion constructs in transgenic
868 analysis of plants. *Biosci Biotechnol Biochem* **71**, 2095-2100 (2007).
869 5. S. J. Clough, A. F. Bent, Floral dip: a simplified method for
870 Agrobacterium-mediated transformation of Arabidopsis thaliana. *Plant*
871 *J* **16**, 735-743 (1998).
872 6. C. Koncz, J. Schell, The promoter of TL-DNA gene 5 controls the
873 tissue-specific expression of chimaeric genes carried by a novel type of
874 Agrobacterium binary vector. *Molecular and General Genetics MGG*
875 **204**, 383-396 (1986).
876 7. F. Jacob *et al.*, A dominant-interfering camta3 mutation compromises
877 primary transcriptional outputs mediated by both cell surface and
878 intracellular immune receptors in Arabidopsis thaliana. *New Phytol* **217**,
879 1667-1680 (2018).
880 8. P. Bucher, K. Karplus, N. Moeri, K. Hofmann, A flexible motif search
881 technique based on generalized profiles. *Comput Chem* **20**, 3-23
882 (1996).
883 9. K. Katoh, K. Misawa, K. Kuma, T. Miyata, MAFFT: a novel method for
884 rapid multiple sequence alignment based on fast Fourier transform.
885 *Nucleic Acids Res* **30**, 3059-3066 (2002).
886 10. J. Soding, Protein homology detection by HMM-HMM comparison.
887 *Bioinformatics* **21**, 951-960 (2005).
888 11. D. Lapin *et al.*, A coevolved EDS1-SAG101-NRG1 module mediates
889 cell death signaling by TIR-domain immune receptors. *bioRxiv*, 572826
890 (2019).
891 12. T. Maekawa *et al.*, Subfamily-Specific Specialization of RGH1/MLA
892 Immune Receptors in Wild Barley. *Mol Plant Microbe Interact* **32**, 107-
893 119 (2019).
894 13. S. Q. Zheng *et al.*, MotionCor2: anisotropic correction of beam-induced
895 motion for improved cryo-electron microscopy. *Nat Methods* **14**, 331-
896 332 (2017).
897 14. A. Rohou, N. Grigorieff, CTFFIND4: Fast and accurate defocus
898 estimation from electron micrographs. *J Struct Biol* **192**, 216-221
899 (2015).
900 15. J. Zivanov *et al.*, New tools for automated high-resolution cryo-EM
901 structure determination in RELION-3. *Elife* **7**, (2018).
902 16. A. Brown *et al.*, Tools for macromolecular model building and
903 refinement into electron cryo-microscopy reconstructions. *Acta*
904 *Crystallogr D Biol Crystallogr* **71**, 136-153 (2015).

905 17. P. D. Adams *et al.*, PHENIX: a comprehensive Python-based system
906 for macromolecular structure solution. *Acta Crystallogr D Biol*
907 *Crystallogr* **66**, 213-221 (2010).
908 18. L. Su *et al.*, A plug release mechanism for membrane permeation by
909 MLKL. *Structure* **22**, 1489-1500 (2014).
910 19. J. M. Murphy *et al.*, The pseudokinase MLKL mediates necroptosis via
911 a molecular switch mechanism. *Immunity* **39**, 443-453 (2013).
912 20. I. M. Saur *et al.*, Multiple pairs of allelic MLA immune receptor-powdery
913 mildew AVRA effectors argue for a direct recognition mechanism. *Elife*
914 **8**, (2019).
915 21. T. Maekawa *et al.*, Coiled-coil domain-dependent homodimerization of
916 intracellular barley immune receptors defines a minimal functional
917 module for triggering cell death. *Cell Host Microbe* **9**, 187-199 (2011).
918 22. F. Vogler, S. S. Konrad, S. Sprunck, Knockin' on pollen's door: live cell
919 imaging of early polarization events in germinating Arabidopsis pollen.
920 *Front Plant Sci* **6**, 246 (2015).
921 23. T. Hamada *et al.*, Purification and characterization of novel
922 microtubule-associated proteins from Arabidopsis cell suspension
923 cultures. *Plant Physiol* **163**, 1804-1816 (2013).
924 24. S. Fujita *et al.*, An atypical tubulin kinase mediates stress-induced
925 microtubule depolymerization in Arabidopsis. *Curr Biol* **23**, 1969-1978
926 (2013).
927 25. C. Gehl *et al.*, Quantitative analysis of dynamic protein-protein
928 interactions in planta by a floated-leaf luciferase complementation
929 imaging (FLuCI) assay using binary Gateway vectors. *Plant J* **67**, 542-
930 553 (2011).
931 26. S. D. Yoo, Y. H. Cho, J. Sheen, Arabidopsis mesophyll protoplasts: a
932 versatile cell system for transient gene expression analysis. *Nat Protoc*
933 **2**, 1565-1572 (2007).
934 27. R. Wessling, R. Panstruga, Rapid quantification of plant-powdery
935 mildew interactions by qPCR and conidiospore counts. *Plant Methods*
936 **8**, 35 (2012).
937 28. A. Cabral *et al.*, Identification of Hyaloperonospora arabidopsidis
938 transcript sequences expressed during infection reveals isolate-specific
939 effectors. *PLoS One* **6**, e19328 (2011).
940 29. S. Bai *et al.*, Structure-function analysis of barley NLR immune
941 receptor MLA10 reveals its cell compartment specific activity in cell
942 death and disease resistance. *PLoS Pathog* **8**, e1002752 (2012).
943 30. R. P. Birkenbihl, C. Diezel, I. E. Somssich, Arabidopsis WRKY33 is a
944 key transcriptional regulator of hormonal and metabolic responses
945 toward Botrytis cinerea infection. *Plant Physiol* **159**, 266-285 (2012).
946 31. C. Gachon, P. Saindrenan, Real-time PCR monitoring of fungal
947 development in Arabidopsis thaliana infected by Alternaria brassicicola
948 and Botrytis cinerea. *Plant Physiol Biochem* **42**, 367-371 (2004).
949 32. Q. H. Shen *et al.*, Recognition specificity and RAR1/SGT1 dependence
950 in barley Mla disease resistance genes to the powdery mildew fungus.
951 *Plant Cell* **15**, 732-744 (2003).
952 33. J. Marc *et al.*, A GFP-MAP4 reporter gene for visualizing cortical
953 microtubule rearrangements in living epidermal cells. *Plant Cell* **10**,
954 1927-1940 (1998).

34. J. Riedl *et al.*, Lifeact: a versatile marker to visualize F-actin. *Nat Methods* **5**, 605-607 (2008).

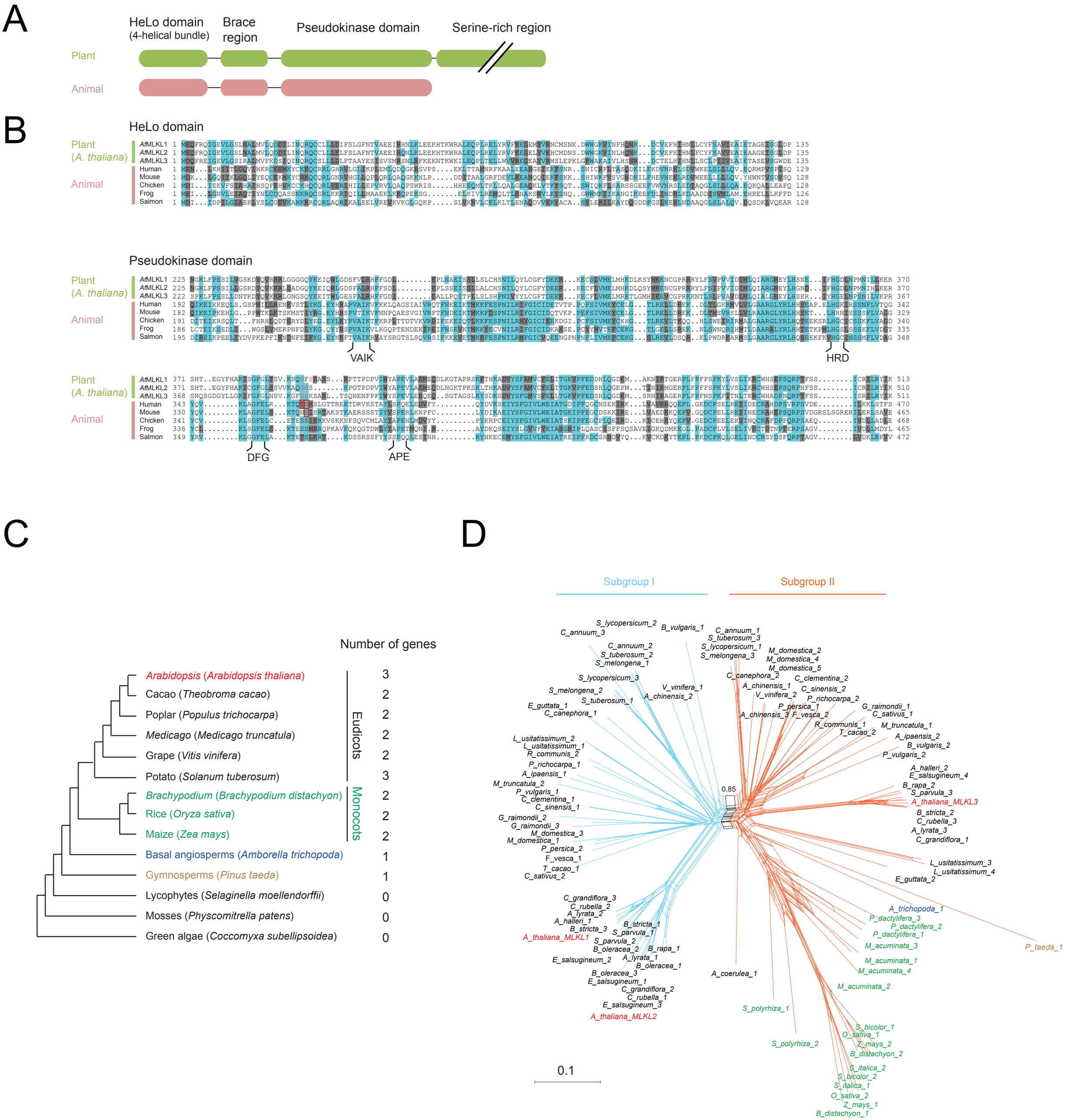
A
HeLo domain
(4-helical bundle)
Brace region
Pseudokinase domain
Serine-rich region
Plant
Animal
B
HeLo domain
Pseudokinase domain
Plant (A. thaliana)
Animal
VAIK
HRD
DFG
APE
C
Number of genes
Arabidopsis (Arabidopsis thaliana) 3
Cacao (Theobroma cacao) 2
Poplar (Populus trichocarpa) 2
Medicago (Medicago truncatula) 2
Grape (Vitis vinifera) 2
Potato (Solanum tuberosum) 3
Brachypodium (Brachypodium distachyon) 2
Rice (Oryza sativa) 2
Maize (Zea mays) 2
Basal angiosperms (Amborella trichopoda) 1
Gymnosperms (Pinus taeda) 1
Lycophytes (Selaginella moellendorffii) 0
Mosses (Physcomitrella patens) 0
Green algae (Coccomyxa subellipsoidea) 0
Eudicots
Monocots
D
Subgroup I
Subgroup II
0.85
0.1

Figure 1

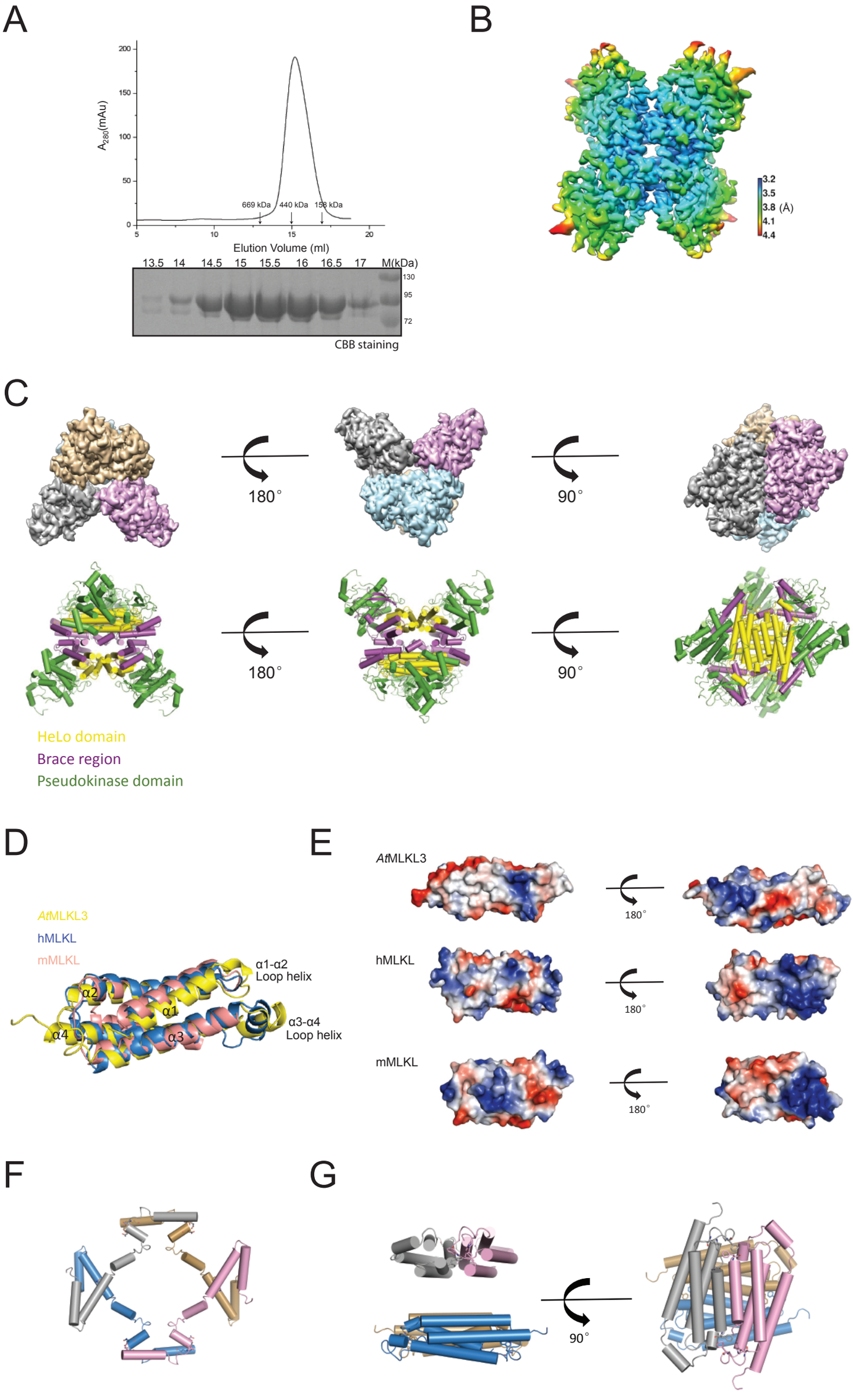
A
200
150
100
50
0
A_{280}(mAu)
669 kDa
440 kDa
158 kDa
5
10
15
20
Elution Volume (ml)
13.5 14 14.5 15 15.5 16 16.5 17 M(kDa)
130
95
72
CBB staining
B
3.2
3.5
3.8 (Å)
4.1
4.4
C
180°
90°
180°
90°
HeLo domain
Brace region
Pseudokinase domain
D
AtMLKL3
hMLKL
mMLKL
α1-α2
Loop helix
α2
α1
α3-α4
Loop helix
α4
α3
E
AtMLKL3
180°
hMLKL
180°
mMLKL
180°
F
G
90°

Figure 2

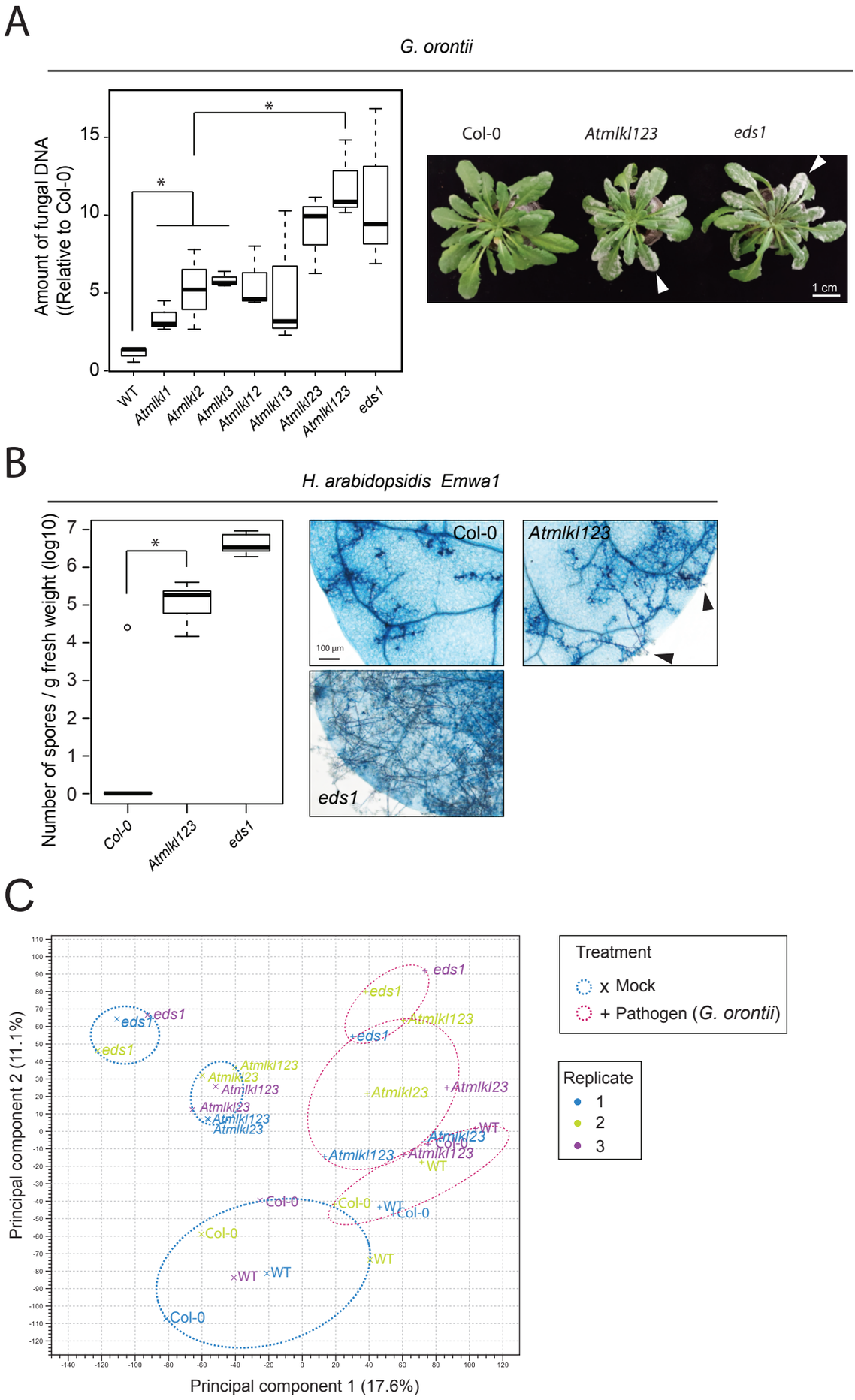
A
G. orontii
Amount of fungal DNA ((Relative to Col-0))
WT
Atmlkl1
Atmlkl2
Atmlkl3
Atmlkl12
Atmlkl13
Atmlkl23
Atmlkl123
eds1
Col-0
Atmlkl123
eds1
1 cm
B
H. arabidopsidis Emwa1
Number of spores / g fresh weight (log10)
Col-0
Atmlkl123
eds1
100 µm
C
Principal component 2 (11.1%)
Principal component 1 (17.6%)
Treatment
x Mock
+ Pathogen (G. orontii)
Replicate
1
2
3

Figure 3

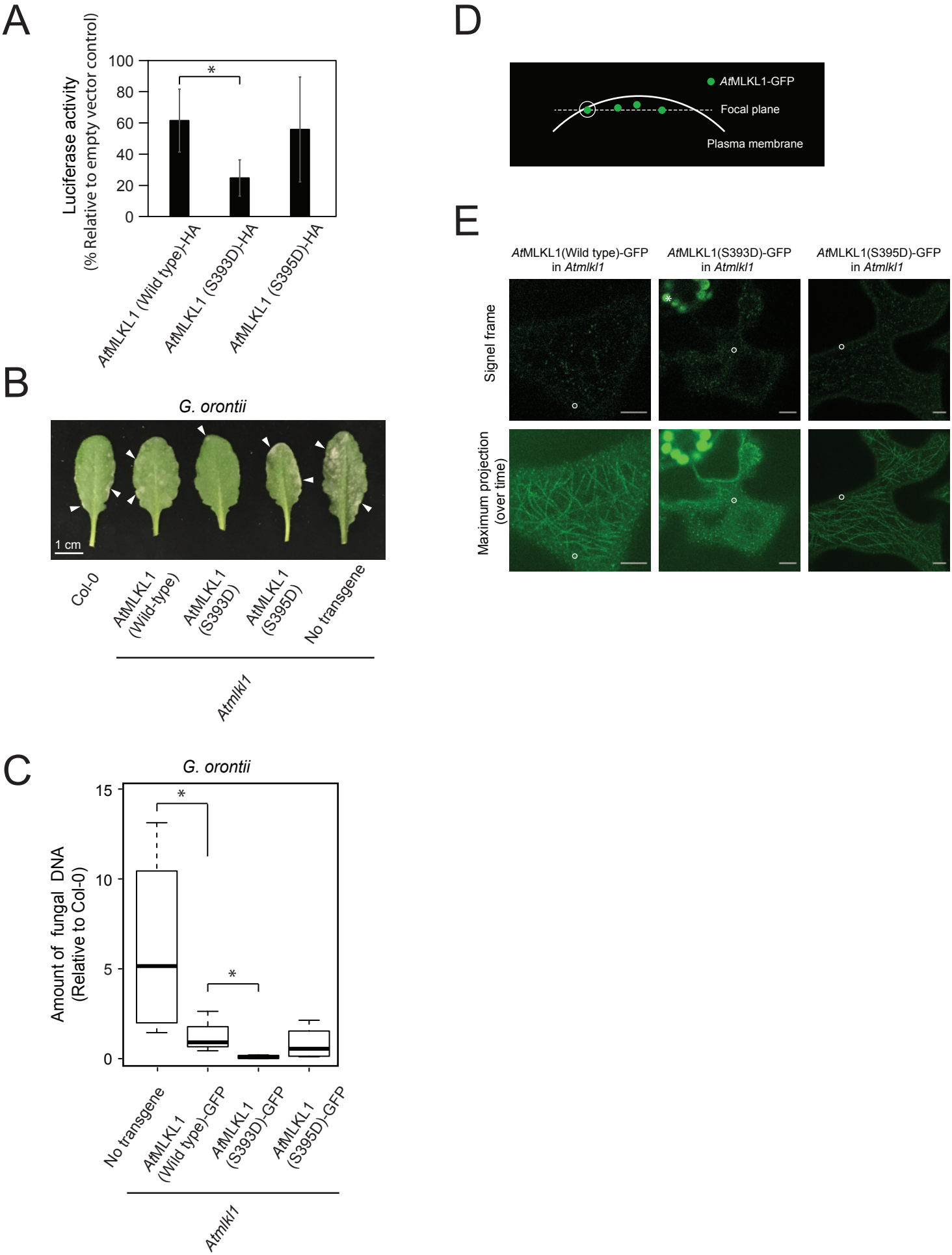
A
Luciferase activity
(% Relative to empty vector control)
100
80
60
40
20
0
*
AtMLKL1 (Wild type)-HA
AtMLKL1 (S393D)-HA
AtMLKL1 (S395D)-HA
B
G. orontii
1 cm
Col-0
AtMLKL1 (Wild-type)
AtMLKL1 (S393D)
AtMLKL1 (S395D)
No transgene
Atmlkl1
C
G. orontii
Amount of fungal DNA
(Relative to Col-0)
15
10
5
0
*
*
No transgene
AtMLKL1 (Wild type)-GFP
AtMLKL1 (S393D)-GFP
AtMLKL1 (S395D)-GFP
Atmlkl1
D
AtMLKL1-GFP
Focal plane
Plasma membrane
E
AtMLKL1(Wild type)-GFP in Atmlkl1
AtMLKL1(S393D)-GFP in Atmlkl1
AtMLKL1(S395D)-GFP in Atmlkl1
Signel frame
Maximum projection (over time)

Figure 4

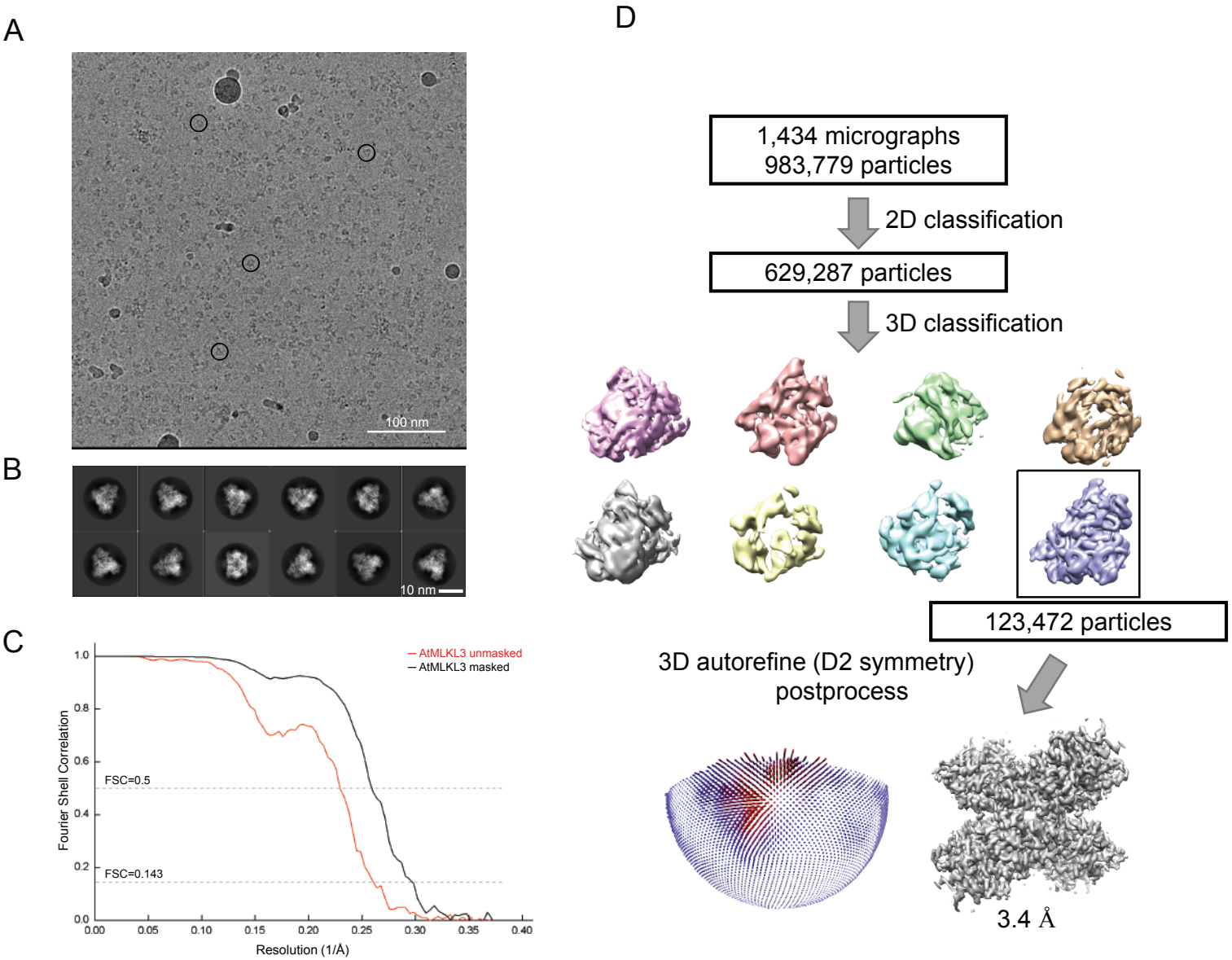
A
100 nm
B
10 nm
C
AtMLKL3 unmasked
AtMLKL3 masked
Fourier Shell Correlation
FSC=0.5
FSC=0.143
Resolution (1/Å)
D
1,434 micrographs
983,779 particles
2D classification
629,287 particles
3D classification
123,472 particles
3D autorefine (D2 symmetry)
postprocess
3.4 Å

Figure S1

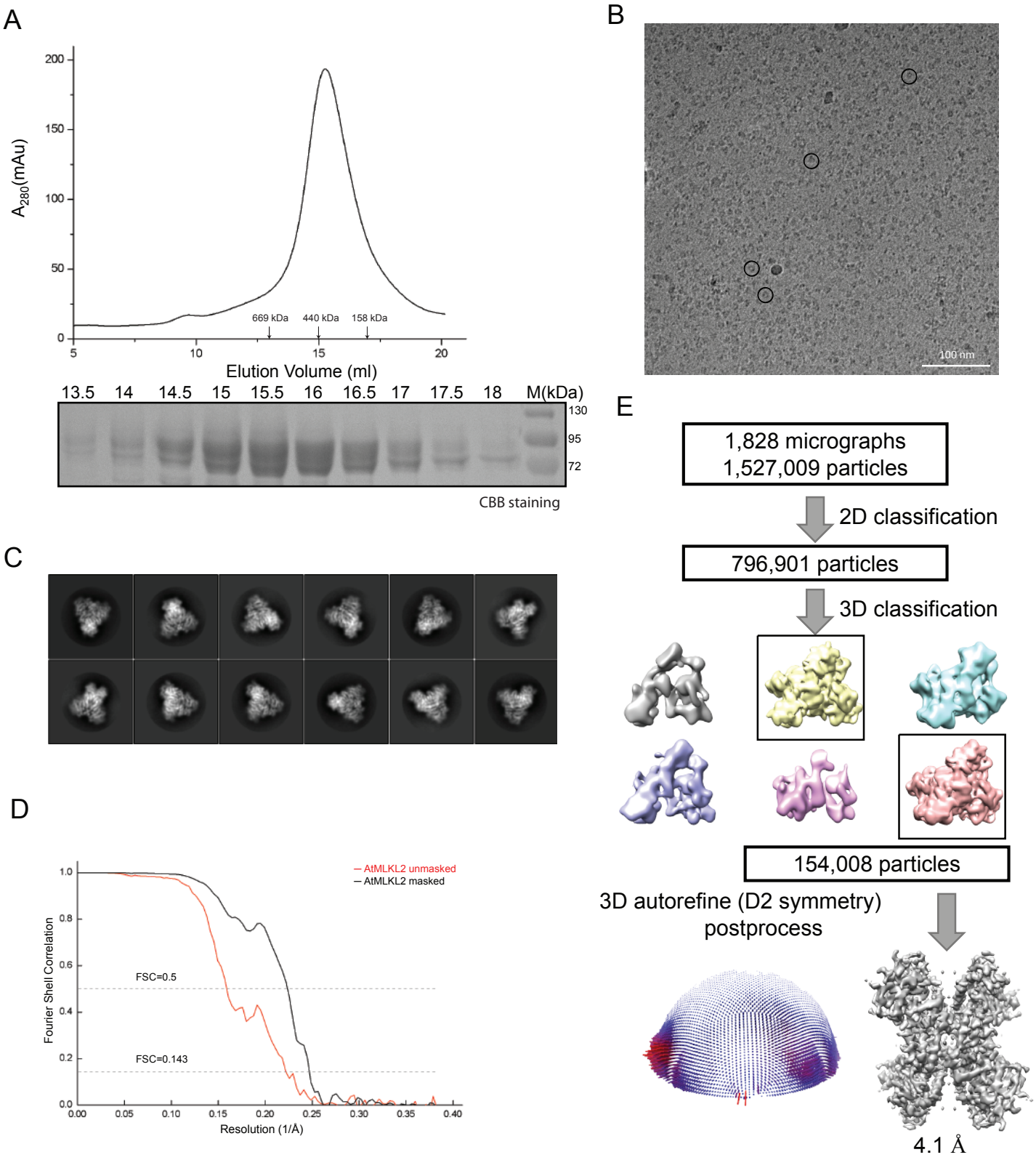
A
A_{280}(mAu)
200
150
100
50
0
5
10
15
20
669 kDa
440 kDa
158 kDa
Elution Volume (ml)
13.5
14
14.5
15
15.5
16
16.5
17
17.5
18
M(kDa)
130
95
72
CBB staining
B
100 nm
C
D
Fourier Shell Correlation
1.0
0.8
0.6
0.4
0.2
0.0
0.00
0.05
0.10
0.15
0.20
0.25
0.30
0.35
0.40
Resolution (1/Å)
AtMLKL2 unmasked
AtMLKL2 masked
FSC=0.5
FSC=0.143
E
1,828 micrographs
1,527,009 particles
2D classification
796,901 particles
3D classification
154,008 particles
3D autorefine (D2 symmetry)
postprocess
4.1 Å

Figure S2

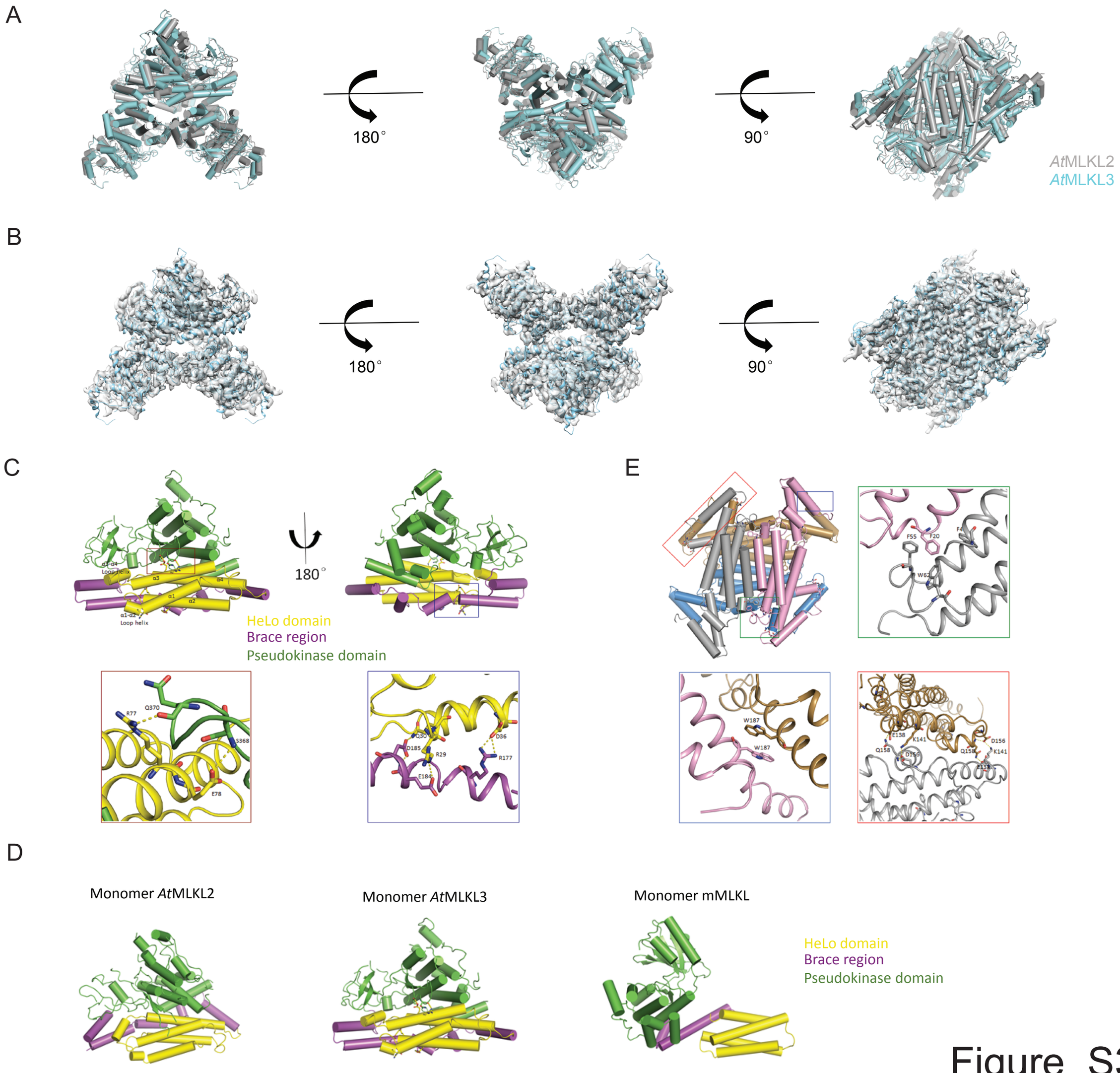
A
180°
90°
AtMLKL2
AtMLKL3
B
180°
90°
C
180°
HeLo domain
Brace region
Pseudokinase domain
E
D
Monomer AtMLKL2
Monomer AtMLKL3
Monomer mMLKL
HeLo domain
Brace region
Pseudokinase domain

Figure S3

A

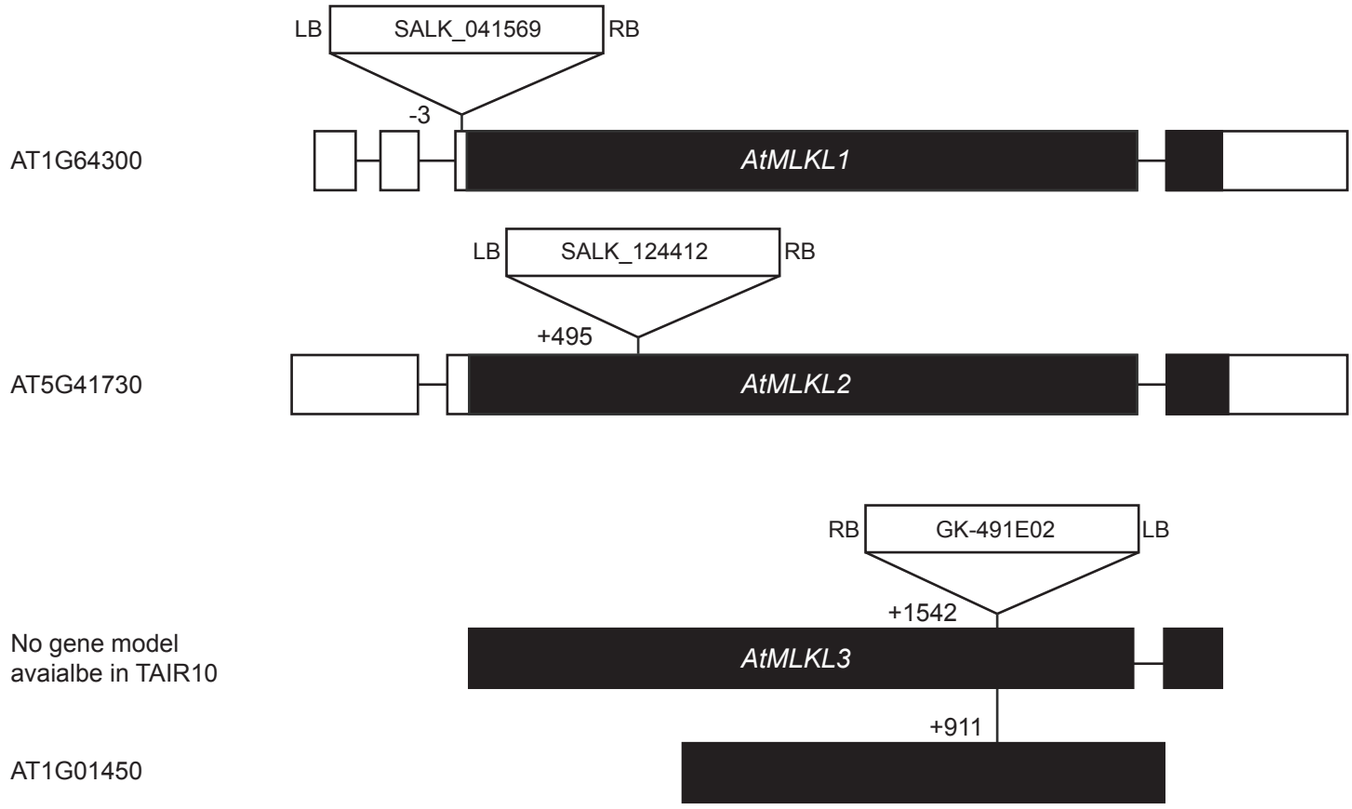
LB
SALK_041569
RB
-3
AT1G64300
AtMLKL1
LB
SALK_124412
RB
+495
AT5G41730
AtMLKL2
RB
GK-491E02
LB
+1542
No gene model
avaialbe in TAIR10
AtMLKL3
+911
AT1G01450

B

1 cm
Col-0
Wild type
Atmlkl1
Atmlkl2
Atmlkl3
1 cm
Atmlkl1 2
Atmlkl1 3
Atmlkl2 3
Atmlkl1 2 3

Figure S4

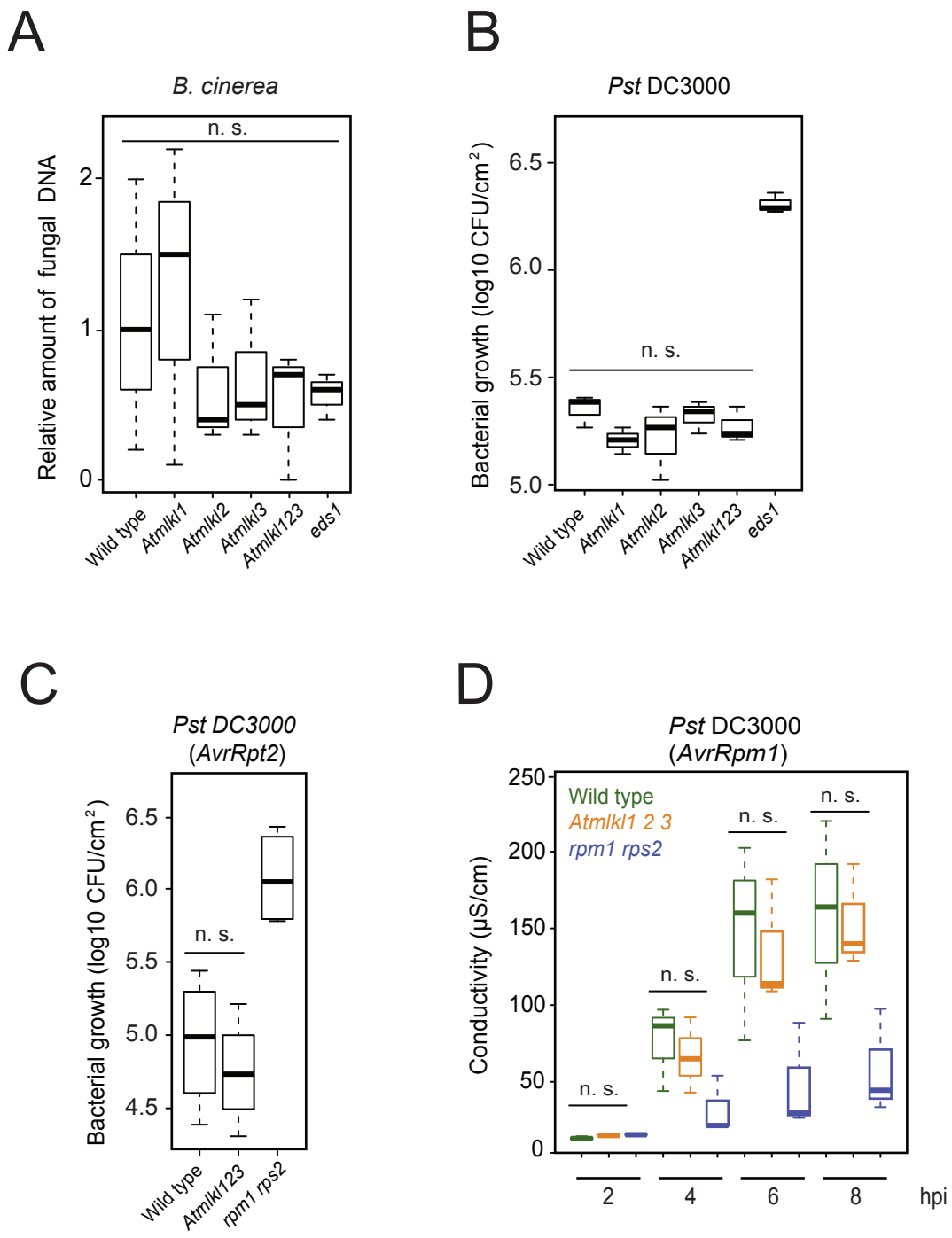
A
B. cinerea
Relative amount of fungal DNA
n. s.
0
1
2
Wild type
Atmlkl1
Atmlkl2
Atmlkl3
Atmlkl123
eds1
B
Pst DC3000
Bacterial growth (log10 CFU/cm2)
n. s.
5.0
5.5
6.0
6.5
Wild type
Atmlkl1
Atmlkl2
Atmlkl3
Atmlkl123
eds1
C
Pst DC3000
(AvrRpt2)
Bacterial growth (log10 CFU/cm2)
n. s.
4.5
5.0
5.5
6.0
6.5
Wild type
Atmlkl123
rpm1 rps2
D
Pst DC3000
(AvrRpm1)
Conductivity (µS/cm)
Wild type
Atmlkl1 2 3
rpm1 rps2
n. s.
n. s.
n. s.
n. s.
0
50
100
150
200
250
2
4
6
8
hpi

Figure S5

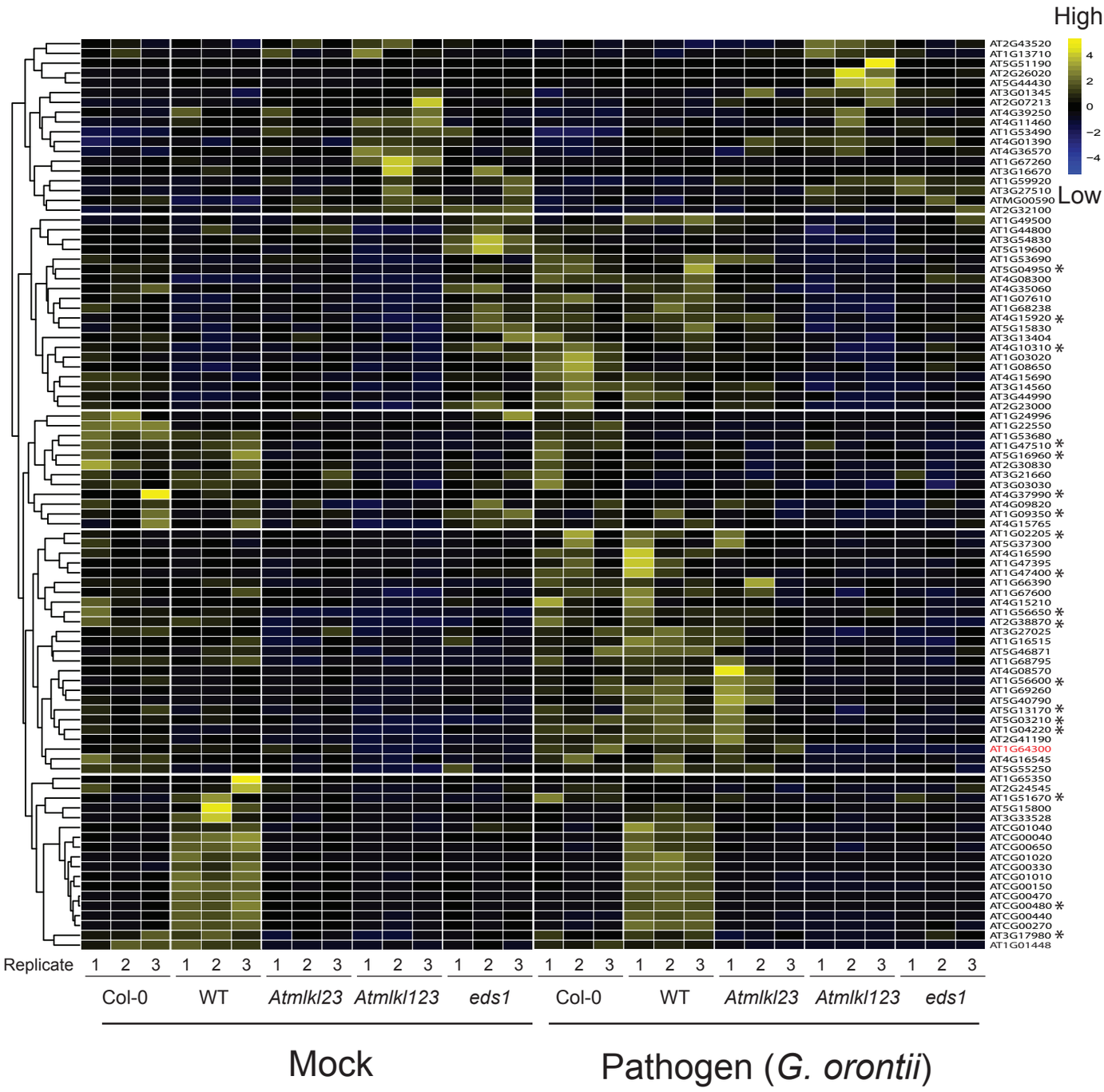
High
Low
4
2
0
−2
−4
Replicate
1 2 3 1 2 3 1 2 3 1 2 3 1 2 3 1 2 3 1 2 3 1 2 3 1 2 3 1 2 3
Col-0
WT
Atmlkl23
Atmlkl123
eds1
Col-0
WT
Atmlkl23
Atmlkl123
eds1
Mock
Pathogen (G. orontii)

Figure S6

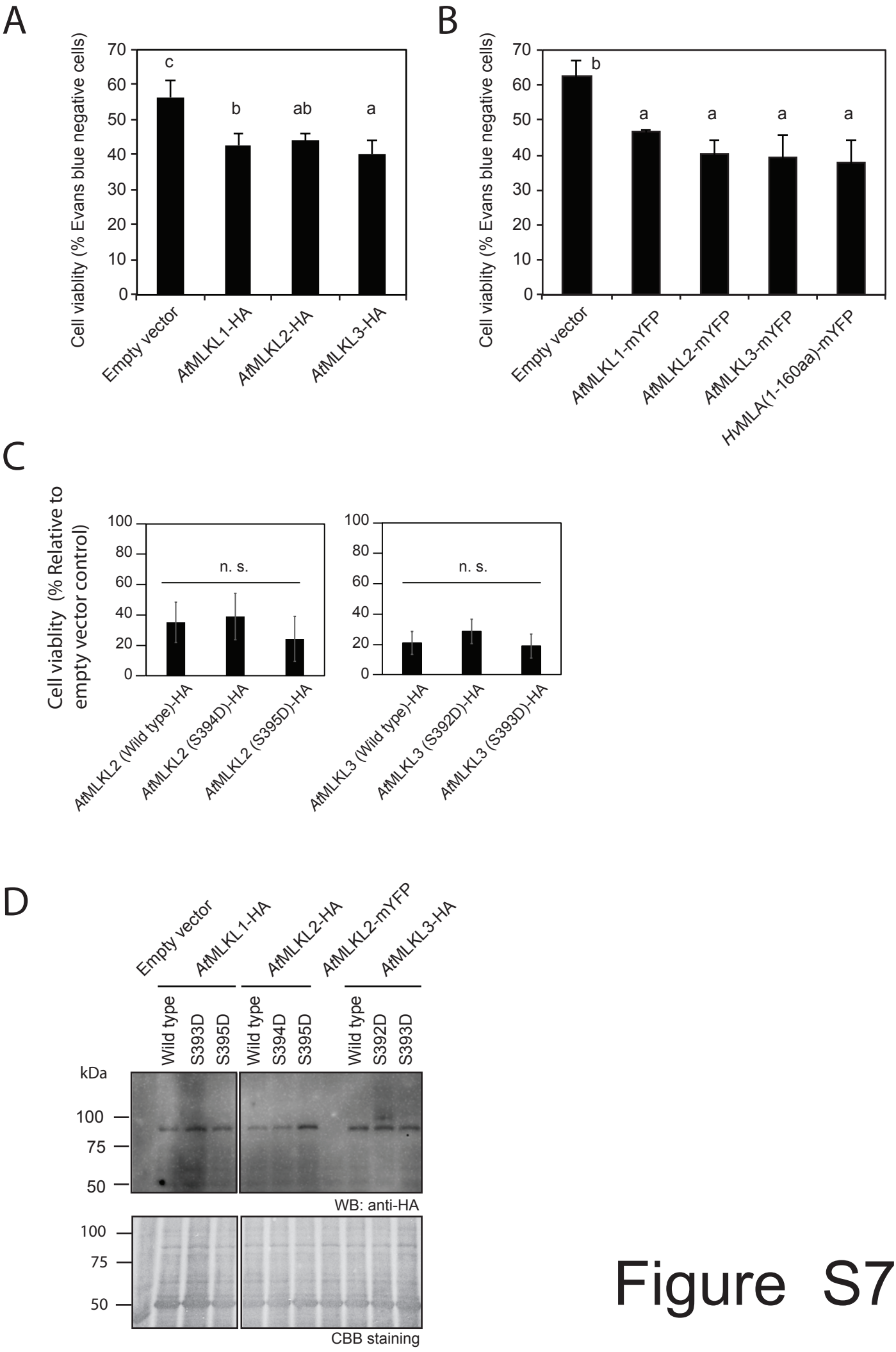
A
Cell viability (% Evans blue negative cells)
70
60
50
40
30
20
10
0
c
b
ab
a
Empty vector
AtMLKL1-HA
AtMLKL2-HA
AtMLKL3-HA
B
Cell viability (% Evans blue negative cells)
b
a
a
a
a
Empty vector
AtMLKL1-mYFP
AtMLKL2-mYFP
AtMLKL3-mYFP
HvMLA(1-160aa)-mYFP
C
Cell viablity (% Relative to empty vector control)
100
80
60
40
20
0
n. s.
AtMLKL2 (Wild type)-HA
AtMLKL2 (S394D)-HA
AtMLKL2 (S395D)-HA
AtMLKL3 (Wild type)-HA
AtMLKL3 (S392D)-HA
AtMLKL3 (S393D)-HA
D
Empty vector
AtMLKL1-HA
AtMLKL2-HA
AtMLKL2-mYFP
AtMLKL3-HA
Wild type
S393D
S395D
Wild type
S394D
S395D
Wild type
S392D
S393D
kDa
100
75
50
WB: anti-HA
CBB staining

Figure S7

A

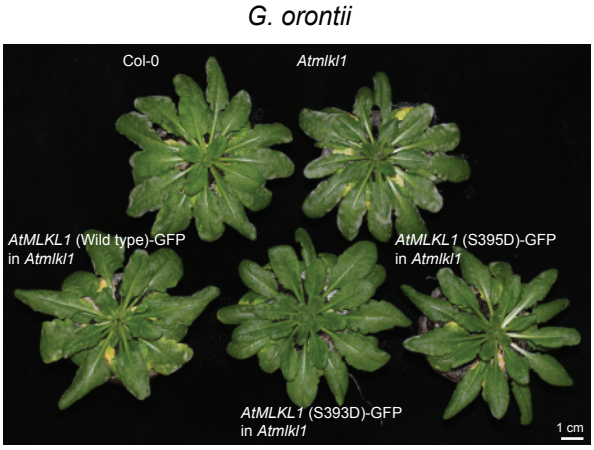
G. orontii
Col-0
Atmlkl1
AtMLKL1 (Wild type)-GFP
in Atmlkl1
AtMLKL1 (S395D)-GFP
in Atmlkl1
AtMLKL1 (S393D)-GFP
in Atmlkl1
1 cm

B

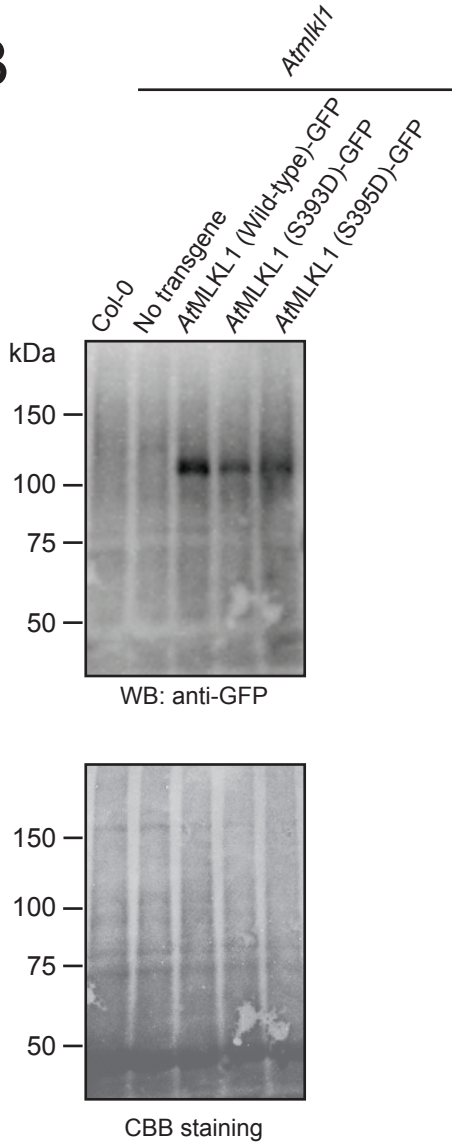
Atmlkl1
Col-0
No transgene
AtMLKL1 (Wild-type)-GFP
AtMLKL1 (S393D)-GFP
AtMLKL1 (S395D)-GFP
kDa
150
100
75
50
WB: anti-GFP
150
100
75
50
CBB staining

Figure S8

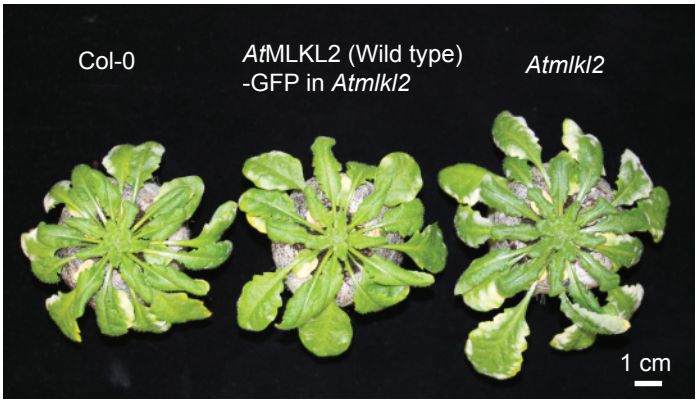
A
Col-0
AtMLKL2 (Wild type)
-GFP in Atmlkl2
Atmlkl2
1 cm

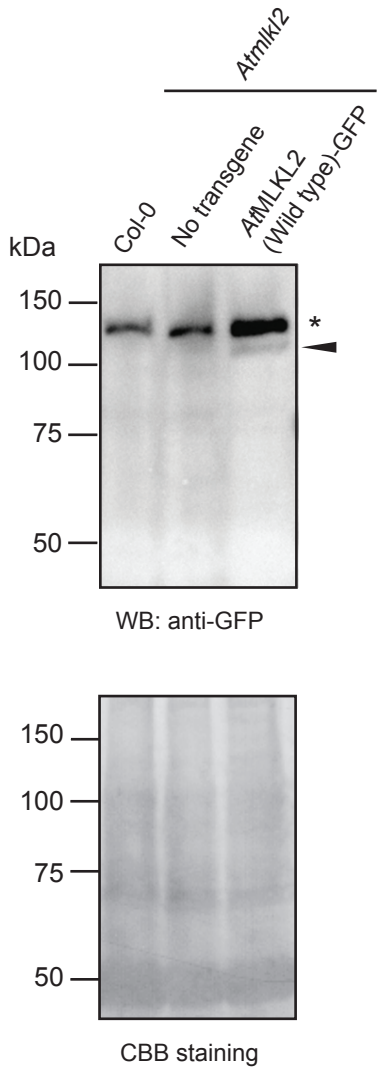
B
Atmlkl2
Col-0
No transgene
AtMLKL2
(Wild type)-GFP
kDa
150
100
75
50
*
WB: anti-GFP
150
100
75
50
CBB staining

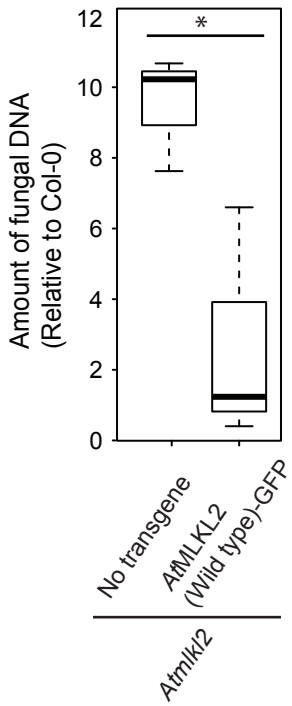
C
Amount of fungal DNA
(Relative to Col-0)
12
10
8
6
4
2
0
*
No transgene
AtMLKL2
(Wild type)-GFP
Atmlkl2

Figure S9

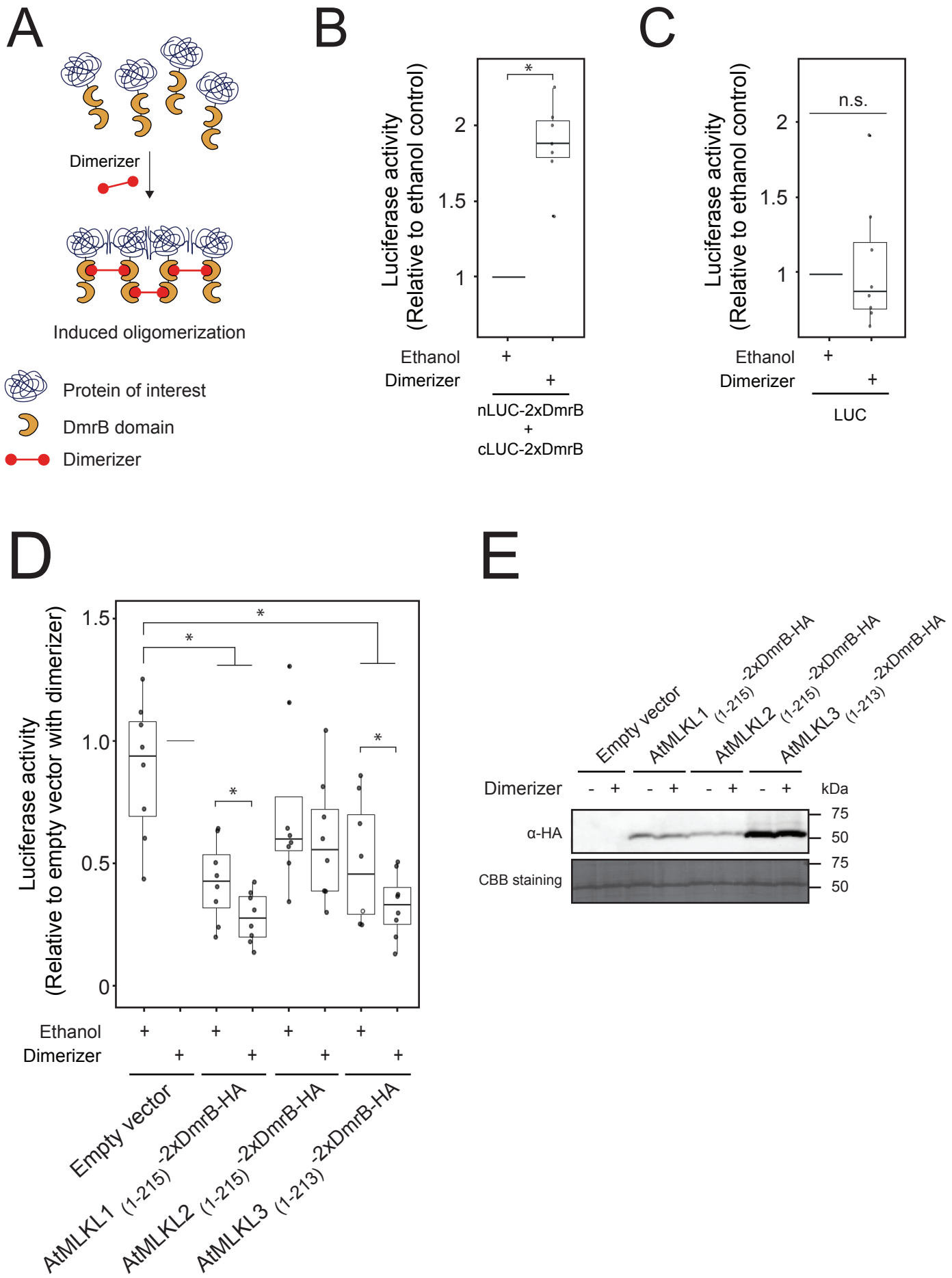
A
Dimerizer
Induced oligomerization
Protein of interest
DmrB domain
Dimerizer
B
Luciferase activity
(Relative to ethanol control)
2
1.5
1
*
Ethanol +
Dimerizer +
nLUC-2xDmrB
+
cLUC-2xDmrB
C
Luciferase activity
(Relative to ethanol control)
2
1.5
1
n.s.
Ethanol +
Dimerizer +
LUC
D
Luciferase activity
(Relative to empty vector with dimerizer)
1.5
1.0
0.5
0
*
Ethanol + + + +
Dimerizer + + + +
Empty vector
AtMLKL1 (1-215) -2xDmrB-HA
AtMLKL2 (1-215) -2xDmrB-HA
AtMLKL3 (1-213) -2xDmrB-HA
E
Empty vector
AtMLKL1 (1-215) -2xDmrB-HA
AtMLKL2 (1-215) -2xDmrB-HA
AtMLKL3 (1-213) -2xDmrB-HA
Dimerizer - + - + - + - +
kDa
α-HA
75
50
CBB staining
75
50

Figure S10

A

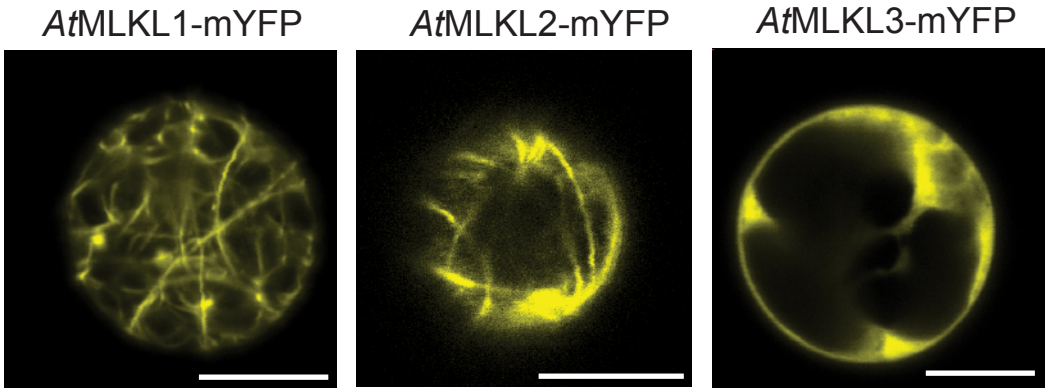

B

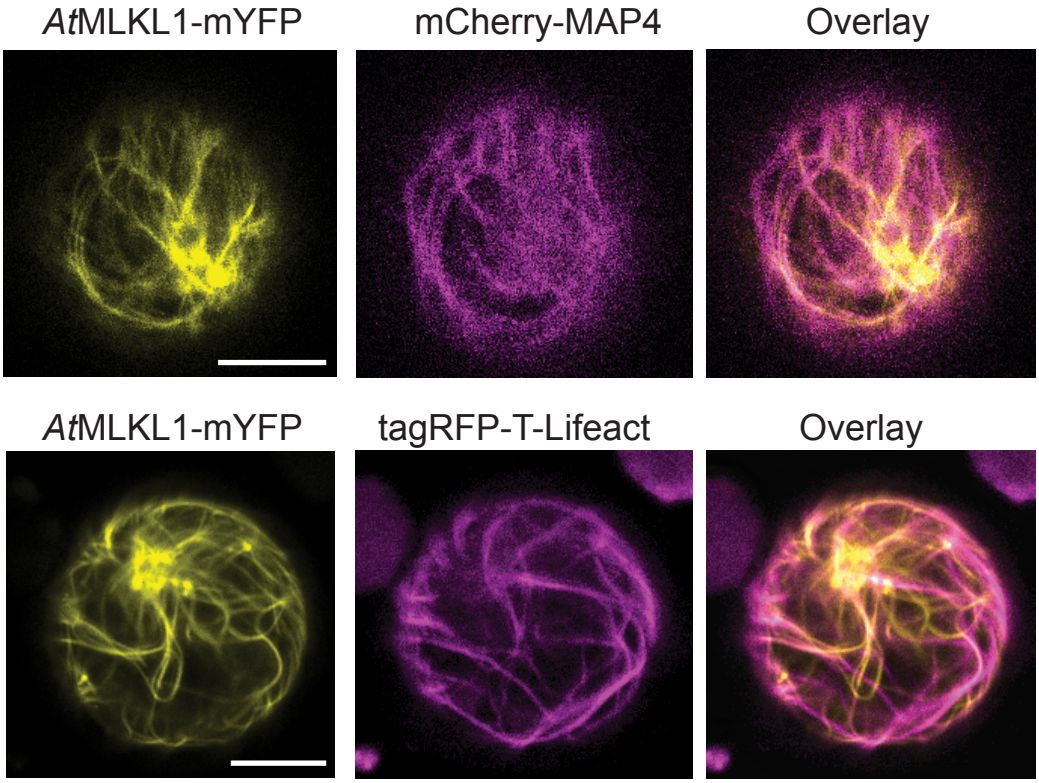

C

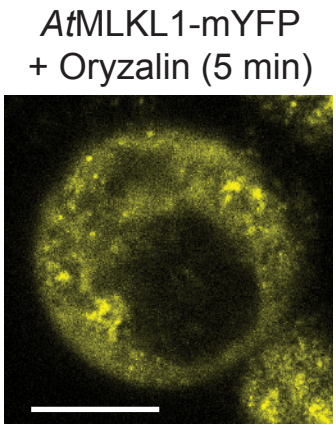

Figure S11

*At*MLKL1(Wild type)-GFP in *Atmlkl1*

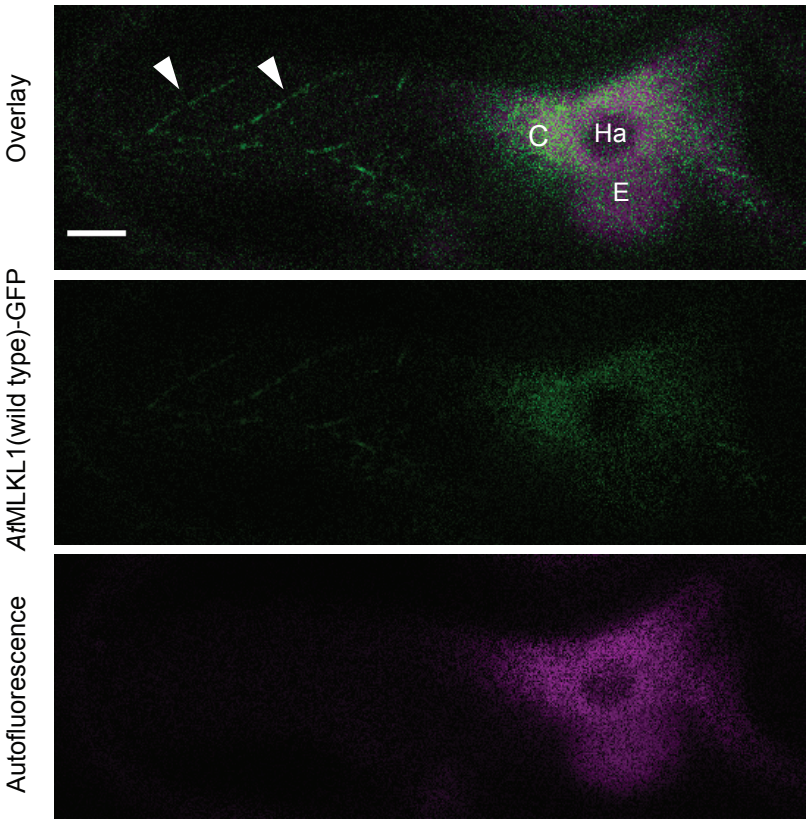

Maximum projection (over Z)

Figure S12

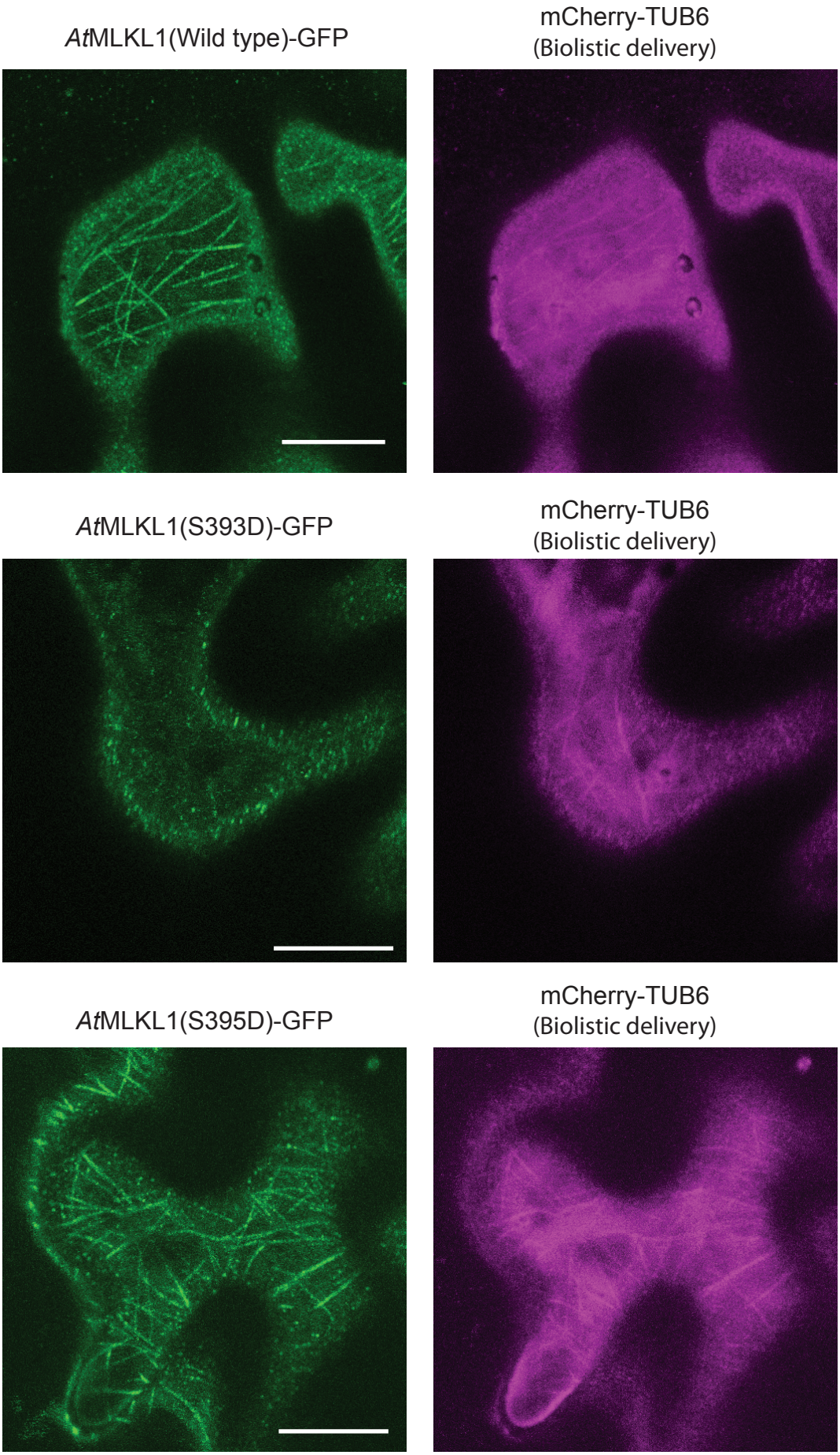
*At*MLKL1(Wild type)-GFP
mCherry-TUB6
(Biolistic delivery)
*At*MLKL1(S393D)-GFP
mCherry-TUB6
(Biolistic delivery)
*At*MLKL1(S395D)-GFP
mCherry-TUB6
(Biolistic delivery)

Figure S13